Anxiety-Related Frontocortical Activity Is Associated With Dampened Stressor Reactivity in the Real World

Juyoen Hur[1], Manuel Kuhn[2], Shannon E. Grogans[3],
Allegra S. Anderson[4], Samiha Islam[5], Hyung Cho Kim[3,6],
Rachael M. Tillman[3], Andrew S. Fox[7,8], Jason F. Smith[3],
Kathryn A. DeYoung[3], and Alexander J. Shackman[3,6,9]

[1]Department of Psychology, Yonsei University; [2]Center for Depression, Anxiety and Stress Research,
McLean Hospital, Harvard Medical School, Harvard University; [3]Department of Psychology, University of
Maryland; [4]Department of Psychological Sciences, Vanderbilt University; [5]Department of Psychology, University
of Pennsylvania; [6]Neuroscience and Cognitive Science Program, University of Maryland; [7]Department of
Psychology, University of California, Davis; [8]California National Primate Research Center, University of
California, Davis; and [9]Maryland Neuroimaging Center, University of Maryland, College Park

Abstract

Negative affect is a fundamental dimension of human emotion. When extreme, it contributes to a variety of adverse outcomes, from physical and mental illness to divorce and premature death. Mechanistic work in animals and neuroimaging research in humans and monkeys have begun to reveal the broad contours of the neural circuits governing negative affect, but the relevance of these discoveries to everyday distress remains incompletely understood. Here, we used a combination of approaches—including neuroimaging assays of threat anticipation and emotional-face perception and more than 10,000 momentary assessments of emotional experience—to demonstrate that individuals who showed greater activation in a cingulo-opercular circuit during an anxiety-eliciting laboratory paradigm experienced lower levels of stressor-dependent distress in their daily lives (ns = 202–208 university students). Extended amygdala activation was not significantly related to momentary negative affect. These observations provide a framework for understanding the neurobiology of negative affect in the laboratory and in the real world.

Negative affect is a fundamental dimension of mammalian emotion. It encompasses transient states—such as anxiety, fear, sadness, and worry—and persistent tendencies to experience and express negative emotions (Shackman et al., 2016). When extreme or pervasive, negative affect contributes to a panoply of adverse outcomes—from physical and mental illness to divorce and premature death—underscoring the need to develop a better understanding of the underlying neurobiology (Hur et al., 2019).

Mechanistic work in animals and neuroimaging research in humans and monkeys have begun to reveal

the broad contours of the neural systems governing negative affect (Chang et al., 2015; Fox & Shackman, 2019; Kenwood & Kalin, 2021). This work underscores the importance of subcortical regions, including the amygdala, bed nucleus of the stria terminalis (BST), and

Corresponding Authors:
Juyoen Hur, Yonsei University, Department of Psychology
Email: jhur1@yonsei.ac.kr

Alexander J. Shackman, University of Maryland, Department of
Psychology
Email: shackman@umd.edu

periaqueductal gray (PAG). But it also highlights frontocortical regions that are particularly well developed in humans, including the midcingulate cortex (MCC), anterior insula (AI), frontal operculum (FrO), and dorsolateral prefrontal cortex (dlPFC; Hur, Smith, et al., 2020; Shackman et al., 2011; Shackman & Fox, 2021). At present, the relevance of these tantalizing laboratory discoveries to subjective emotional experience in the real world remains incompletely understood. Given the limitations of ambulatory measures of brain activity, overcoming this barrier requires integrating measures of emotion-relevant brain function acquired in the laboratory with assessments of negative affect collected in the field.

Here, we used functional MRI (fMRI) to quantify individual differences in neural reactivity to a well-established anxiety-provocation (threat-anticipation) paradigm in 220 young adults (Fig. 1). A multiband MRI sequence and best-practice data-processing techniques enhanced our ability to resolve small subcortical regions (e.g., amygdala and BST). Next, we used smartphone experience sampling—often termed *ecological momentary assessment* (EMA)—to intensively sample fluctuations in self-reported negative affect and stressor exposure across different real-world contexts. Because EMA data are captured in real time, they circumvent the biases that can distort retrospective reports and provide insights into how emotional experience dynamically responds to everyday stressors. To ensure a broad spectrum of emotional reactivity, we selectively recruited subjects from a pool of 6,594 young adults screened for traitlike individual differences in negative emotionality. We focused on emerging adulthood because it is a time of profound, often stressful transitions (Shackman et al., 2018). In fact, more than half of undergraduate students report moderate-to-severe levels of anxiety and depression, and many experience frank emotional disorders during this turbulent developmental chapter (The National Academies of Sciences, Engineering, and Medicine, 2021; Vos et al., 2020).

A series of hierarchical linear models (HLMs)—sometimes termed multilevel or linear mixed models—was used to fuse the fMRI and EMA data streams (Fig. 1). HLM naturally handles the nested dependency and variable number of assessments completed by each subject, is the standard analytic framework for EMA and other kinds of experience-sampling data, and enabled us to test relations between anxiety-related brain function and *tonic* (stressor-independent) and *reactive* (stressor-dependent) variation in real-world negative affect (Shackman et al., 2016). To clarify specificity, we performed parallel analyses for positive affect and positive events. This analytic framework also allowed us to quantify the added explanatory value (i.e., incremental validity) of neuroimaging metrics relative to conven-

Statement of Relevance

Anxiety, sadness, and other negative emotions are hallmarks of the human condition. When extreme, they contribute to a variety of adverse outcomes—from physical and mental illness to divorce and premature death—pointing to the need to develop a better understanding of the underlying brain circuitry. Recent work has begun to reveal the neural systems governing negative affect, but the relevance of these tantalizing laboratory discoveries to the real world has remained unclear. Here, we used a combination of brain imaging and smartphone survey techniques to show that individuals marked by greater activation in a cingulo-opercular circuit during an anxiety-promoting laboratory paradigm tended to experience diminished distress in response to everyday stressors. These observations provide new insights into the brain systems most relevant to moment-by-moment fluctuations in negative mood, underscoring the importance of more recently evolved cortical association areas.

tional paper-and-pencil measures of trait negative emotionality (Shackman & Fox, 2018).

In addition to addressing the real-world significance of anxiety-related brain circuitry, this approach afforded an opportunity to clarify the contributions of frontocortical regions to negative affect. Although the MCC, AI/FrO, and dlPFC are consistently recruited by a variety of distress-eliciting experimental challenges, their precise role has remained enigmatic (Hur, Smith, et al., 2020). In part, this reflects the fact that a broadly similar network is recruited by emotion-regulation paradigms (Langner et al., 2018; Morawetz et al., 2020), raising the possibility that frontocortical activation actually reflects spontaneous efforts to dampen, rather than promote, distress. Fusing the fMRI and EMA data streams enabled us to test whether frontocortical activity is associated with increased or decreased negative affect in the midst of daily life.

To provide a more direct link with ongoing research, we conducted parallel analyses using fMRI data from a subset of subjects who also completed an emotional-faces paradigm. Variants of the emotional-faces paradigm are widely used as probes of amygdala function—often in the guise of quantifying variation in "negative valence systems"—and have been incorporated into many biobank studies (e.g., Adolescent Brain Cognitive Development, Human Connectome Project, IMAGEN, and UK Biobank). Although photographs of models posing "threat-related" (i.e., fearful and angry) facial
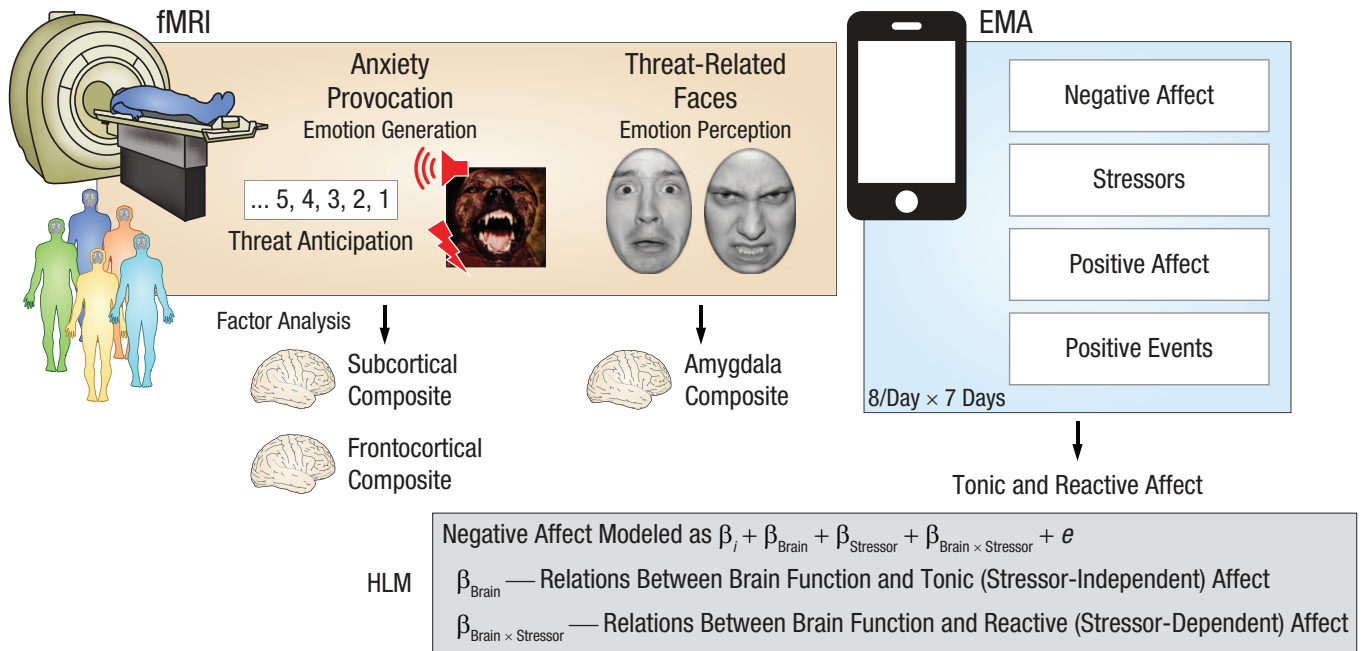
Fig. 1. Study overview. All subjects were assessed using functional MRI (fMRI), a well-established anxiety-provocation paradigm, and ecological momentary assessment (EMA). On threat trials, subjects saw a stream of integers that culminated with the delivery of a noxious electric shock, an unpleasant photograph, and a thematically related audio clip (e.g., growl, scream). Control trials were similar but terminated with the delivery of benign reinforcers. A subset of subjects also completed a threat-related-faces paradigm, during which they viewed photographs of fearful or angry faces. Photographs of neutral outdoor scenes served as a control. To integrate the fMRI and EMA data streams, we defined regions of interest on the basis of significant group-level activation in whole-brain analyses (false discovery rate $q < .05$, whole-brain corrected) within anatomical regions highlighted by prior work using similar tasks. For the anxiety-provocation task, analyses focused on subcortical (amygdala, bed nucleus of the stria terminalis, and periaqueductal gray) and frontocortical (midcingulate cortex, anterior insula, frontal operculum, and dorsolateral prefrontal cortex) activation during threat anticipation. To reduce the number of comparisons and maximize statistical power, we used a factor analysis to guide the construction of composite measures of brain activity. For the faces paradigm, analyses focused on a composite measure of bilateral amygdala activation. Smartphone EMA was used to sample hour-by-hour fluctuations in negative and positive affect. Subjects also reported exposure to stressors and positive events in the past hour, enabling examination of tonic (stressor-independent) and reactive (stressor-dependent) affect. Subjects completed up to eight EMA surveys per day for 7 days, yielding a total of 10,239 usable assessments. A series of hierarchical linear models (HLMs) enabled us to selectively probe relations between the composite neuroimaging metrics derived for each task and tonic and reactive negative affect. A similar approach was used for follow-up tests of specificity and incremental validity.

expressions strongly activate the amygdala (Miller et al., 2016), they do not elicit distress in typical adults and consequently are better conceptualized as a probe of emotion perception rather than as the experience or expression of emotion (Hur et al., 2019). Here, we tested whether differences in amygdala reactivity to threat-related faces are associated with EMA measures of negative affect (Fig. 1).

Discovering the neural systems most relevant to the moment-by-moment experience of negative affect in daily life is important. Emotional illnesses are defined, diagnosed, and treated on the basis of real-world feelings, and for some theorists they are the defining feature of emotion (Fox et al., 2018; Mobbs et al., 2019). This approach has the potential to provide insights that cannot be achieved using either animal models or isolated measures of human brain function and represents a step toward establishing the everyday relevance of the brain circuits highlighted in neuroimaging studies of emotion generation and perception.

Method

Overview

As part of an ongoing prospective longitudinal study focused on the emergence of internalizing disorders, we used measures of trait negative emotionality—often termed neuroticism or dispositional negativity—to screen 6,594 young adults (57.1% female, 42.9% male; 59.0% White, 19.0% Asian, 9.9% African American, 6.3% Hispanic, 5.8% multiracial/other; age: $M = 19.2$ years, $SD = 1.1$; Hur, DeYoung, et al., 2020; Shackman et al., 2018). Screening data were stratified into quartiles (top quartile, middle quartiles, bottom quartile) separately for men and women. Individuals who met preliminary inclusion criteria were independently and randomly recruited from each of the resulting six strata. Given the focus of the larger study, approximately half the subjects were recruited from the top quartile, and the remainder were split between the middle and bottom quartiles (i.e., 50% high, 25% medium, and 25% low),

enabling us to sample a wide range of risk for the development of internalizing disorders. Simulation work suggests that this enrichment approach does not bias statistical tests to a degree that would compromise their validity (Hauner et al., 2014). All subjects were first-year university students in good physical health with normal or corrected-to-normal color vision and access to a personal smartphone. All reported the absence of lifetime neurological or pervasive developmental disorders, MRI contraindications, or prior experience with aversive electrical stimulation. All subjects were free from lifetime psychotic and bipolar disorders; a current mood, anxiety, or trauma disorder (past 2 months); severe substance abuse (i.e., associated with physical disability, hospitalization, or inpatient treatment); active suicidality; and ongoing psychiatric treatment as determined by an experienced master's-level diagnostician using the Structured Clinical Interview for *DSM-5* (First et al., 2015). Subjects with a lifetime history of internalizing disorders were excluded in order to maximize the range of emotional reactivity and psychiatric risk. At the baseline laboratory session, subjects provided informed written consent, were familiarized with the EMA protocol (see below), and recompleted the assessment of trait negative emotionality. Beginning the next day, subjects completed up to eight EMA surveys per day for 7 days (see below). Subjects completed the neuroimaging assessment within 2 to 5 weeks of beginning the EMA protocol (*Mdn* = 13 days, maximum = 39 days). All procedures were approved by the University of Maryland Institutional Review Board. The sample overlaps that featured in prior work by our group focused on social anxiety (Hur, DeYoung, et al., 2020) and the basic neurobiology of threat processing (Hur, Smith, et al., 2020).

Subjects

A total of 234 subjects completed the MRI assessment.

Anxiety provocation. Fourteen subjects were excluded from fMRI analyses of the anxiety-provocation task because of incidental neurological findings (*n* = 4), scanner problems (*n* = 2), insufficient usable fMRI data (*n* = 2; see below), or excessive global motion artifacts (*n* = 6; see below). Twelve subjects did not successfully complete the EMA assessment (see below) and were excluded from fMRI–EMA analyses. This yielded a final sample of 208 subjects (50.0% female, 50.0% male; 63.0% White, 17.3% Asian, 8.2% African American, 3.8% Hispanic, 7.7% multiracial/other; age: *M* = 18.8 years, *SD* = 0.4).

Threat-related faces. Twenty-one subjects were excluded from fMRI analyses of the threat-related-faces task because

of incidental neurological findings (*n* = 4), scanner problems (*n* = 2), gross artifacts (*n* = 1), insufficient usable fMRI data (*n* = 1; see below), excessive global motion artifacts (*n* = 7; see below), or inadequate performance accuracy (*n* = 6; see below). Eleven subjects did not successfully complete the EMA assessment (see below) and were excluded from fMRI–EMA analyses. This yielded a final sample of 202 subjects (50.0% female, 50.0% male; 63.4% White, 16.8% Asian, 8.4% African American, 4.0% Hispanic, 7.4% multiracial/other; age: *M* = 18.8 years, *SD* = 0.4).

Power analysis

Sample size was determined a priori as part of the application for the award that supported data collection (R01-MH107444). The target sample size (*N* ≈ 240) was chosen to afford acceptable power and precision given available resources (Schönbrodt & Perugini, 2013). At the time of study design, G*Power (Version 3.1.9.2; Faul et al., 2007) indicated that this sample size would provide greater than 99% power to detect a benchmark medium-sized effect (*r* = .30) with up to 20% planned attrition (*N* = 192 usable data sets) using an α of .05 (two-tailed).

Trait negative emotionality

As in prior work by our group (Hur, DeYoung, et al., 2020; Shackman et al., 2018), we used measures of neuroticism (Big Five Inventory–Neuroticism, α = .86; John et al., 2008) and trait anxiety (International Personality Item Pool-Trait Anxiety, α = .89; Goldberg et al., 2006) to quantify stable individual differences in negative emotionality. Subjects used a 5-point scale (1, *disagree strongly*, to 5, *agree strongly*) to rate themselves on a total of 18 items (e.g., "depressed or blue," "tense," "worry," "nervous," "get distressed easily," "fear for the worst," "afraid of many things"). To minimize the influence of occasion-specific fluctuations in responding, we created an average measure using the screening and baseline assessments (median interval = 80.0 days, *SD* = 56.6). The resulting multiscale, multi-occasion composite captured a sizable spectrum of trait negative emotionality (*z* = −2.11–1.49) and showed acceptable reliability (α = .93, test-retest reliability: *r* = .75).

General neuroimaging procedures

Prior to scanning, subjects practiced abbreviated versions of the tasks until staff confirmed their understanding. A detailed description of the peripheral apparatus is available in Hur, Smith, et al. (2020). During imaging, foam inserts were used to mitigate potential motion artifacts. Subjects were continuously monitored using

an MRI-compatible eye tracker (EyeLink 1000; SR Research, Ottawa, Ontario, Canada) and a near real-time head-motion monitor. Following the last scan, subjects were removed from the scanner, debriefed, compensated, and discharged.

Anxiety-provocation paradigm

Paradigm structure and procedures. The anxiety-provocation (threat-anticipation) paradigm is schematically depicted in Figure S1 in the Supplemental Material available online. A detailed description of the paradigm and associated procedures and stimuli is available in Hur, Smith, et al. (2020). Subjects were informed about the task design and contingencies prior to scanning. The task was administered in three scans (12 trials per valence per scan). On threat trials, subjects saw a stream of integers ($M = 18.75$ s; range = 8.75–30.00 s). To ensure robust anticipatory anxiety, we ensured that this epoch always culminated with the delivery of a noxious electric shock, an unpleasant photograph (e.g., mutilated body), and a thematically related audio clip (e.g., scream, gunshot). Safety trials were similar but terminated with the delivery of benign reinforcers (i.e., just-perceptible electrical stimulation and neutral audiovisual stimuli). Valence was continuously signaled during the anticipation epoch by the background color of the display. White-noise visual masks (3.2 s) were presented between trials to minimize persistence of the visual reinforcers in iconic memory. Subjects were periodically prompted to rate the intensity of negative affect (fear/anxiety) experienced a few seconds earlier, during the anticipation period of the prior trial, using a 4-point scale (1, *minimal*, to 4, *maximal*).

Skin conductance data acquisition and processing. To confirm the validity of the anxiety-provocation paradigm, we continuously assessed skin conductance during each scan of the anxiety-provocation task using a BIOPAC system (MP-150; BIOPAC Systems, Goleta, CA). Skin conductance (250 Hz; 0.05 Hz high-pass filter) was measured using MRI-compatible disposable electrodes (EL507) attached to the second and third fingers of the nondominant hand. Skin conductance data were processed using *PsPM* (Version 4.0.2; Bach & Friston, 2013) and in-house MATLAB code (The MathWorks, Natick, MA). Data from each scan were band-pass filtered (0.01–0.25 Hz), resampled to match the repetition time (TR) used for fMRI data acquisition (1.25 s), and *z*-transformed.

Threat-related-faces paradigm

The threat-related-faces paradigm is schematically depicted in Figure S2 in the Supplemental Material. The paradigm had a pseudorandomized block design and was administered in two scans with a short break between scans. During each scan, subjects viewed photographs of models depicting angry faces, fearful faces, happy faces, or places (seven blocks per condition per scan). Blocks consisted of 10 photographs (1.6 s) separated by fixation crosses (0.4 s). Subjects were instructed to judge whether the current photograph matched that presented on the prior trial (i.e., a "1-back" continuous performance task) in order to maximize task engagement. Place stimuli consisted of photographs of outdoor scenes focused on single-family residential buildings (houses) or urban commercial buildings (skyscrapers). A total of six additional echo-planar imaging (EPI) volumes were acquired at the beginning and end of each scan (see below). Subjects with inadequate performance (i.e., accuracy < 2 *SD* for both scans) were excluded from analyses.

MRI data acquisition

MRI data were acquired using a Siemens Magnetom TIM Trio 3-tesla scanner (32-channel head coil). Sagittal T1-weighted anatomical images were acquired using a magnetization-prepared rapid-acquisition gradient echo (MPRAGE) sequence (TR = 2,400 ms, echo time [TE] = 2.01 ms, inversion time = 1,060 ms, flip angle = 8°, sagittal-slice thickness = 0.8 mm, in-plane resolution = 0.8 × 0.8 mm, matrix = 300 × 320, field of view = 240 × 256). A T2-weighted image was collected at the same location and with the same resolution as the T1-weighted image (TR = 3,200 ms, TE = 564 ms, flip angle = 120°). To enhance resolution, we used a multiband sequence to collect EPI volumes (multiband acceleration = 6, TR = 1,250 ms, TE = 39.4 ms, flip angle = 36.4°, slice thickness = 2.2 mm, number of slices = 60, in-plane resolution = 2.1875 × 2.1875 mm, matrix = 96 × 96). Images were collected in the oblique axial plane (approximately −20° relative to the anterior commissure–posterior commissure plane) to minimize potential susceptibility artifacts (anxiety provocation: 478 volumes per scan; faces: 454 volumes per scan). The first seven volumes were automatically discarded by the scanner. To allow field-map correction, we collected two oblique-axial spin-echo images in opposing phase-encoding directions (rostral-to-caudal and caudal-to-rostral) at the same location and resolution as the EPI volumes (TR = 7,220 ms, TE = 73 ms).

MRI data processing

Methods were optimized to minimize coregistration error and other potential sources of noise. Structural MRI and fMRI data were visually inspected before and after processing for quality assurance.

Anatomical data. Methods were similar to those employed in recent reports by our group (e.g., Hur, Smith, et al., 2020). T1-weighted images were inhomogeneity corrected using *N4* software (Tustison et al., 2010) and filtered using the denoise function in *Advanced Neuroimaging Tools* (*ANTs*; Avants et al., 2011). The brain was then extracted using a variant of *BEaST* software (Eskildsen et al., 2012) with brain-extracted and normalized reference brains from the IXI database (Biomedical Image Analysis Group, 2022). Brain-extracted T1 images were normalized to a version of the brain-extracted 1-mm T1-weighted MNI152 (Version 6) template (Grabner et al., 2006), customized to remove extracerebral tissue. This was motivated by evidence that brain-extracted T1 images and templates enhance the quality of spatial normalization. Normalization was performed using the diffeomorphic approach implemented in *SyN* (Version 1.9.x .2017-09.11; Avants et al., 2011). T2-weighted images were rigidly coregistered with the corresponding T1 prior to normalization, and the brain-extraction mask from the T1 was applied. Tissue priors were unwarped to the native space of each T1 using the inverse of the diffeomorphic transformation (Lorio et al., 2016). Brain-extracted T1 and T2 images were simultaneously segmented using native-space priors generated using *FAST* (FSL Version 5.0.9; Jenkinson et al., 2012) for use in EPI–T1 coregistration (see below).

Field-map data. Spin-echo images were used to create a field map in *topup* software (Jenkinson et al., 2012). Field maps were converted to radians, median-filtered, and smoothed (2 mm). The average of the distortion-corrected spin-echo images was inhomogeneity-corrected using *N4* and brain-masked using *3dSkullStrip* (AFNI Version 17.2.10; Cox, 1996). The resulting mask was minimally eroded to exclude extracerebral voxels.

Functional data. EPI files were despiked (using *3dDespike*; Cox, 1996) and slice-time corrected (to the center of the TR) using *3dTshift* (Cox, 1996), inhomogeneity-corrected using *N4*, and motion-corrected to the first volume using a 12-parameter affine transformation implemented in *ANTs*. Transformations were saved in Insight Toolkit–compatible format for subsequent use (McCormick et al., 2014). The first volume was extracted for EPI–T1 coregistration. The reference EPI volume was simultaneously coregistered with the corresponding T1-weighted image in native space and corrected for geometric distortions using boundary-based registration (Greve & Fischl, 2009). This step incorporated the previously created field map, undistorted spin echo, T1, white-matter image, and masks. The spatial transformations necessary to transform each EPI volume from native space

to the reference EPI, from the reference EPI to the T1, and from the T1 to the template were concatenated and applied to the processed (despiked and slice-time-corrected) EPI data in a single step to minimize incidental spatial blurring. Normalized EPI data were resampled to 2-mm isotropic voxels using fifth-order b splines and then smoothed (6-mm full-width at half maximum) using *3DblurInMask* (Cox, 1996).

EMA protocol, measures, and data reduction

Protocol. *SurveySignal* (Hofmann & Patel, 2015) was used to automatically deliver eight text messages per day to each subject's smartphone. Messages were delivered between 8:30 a.m. and 11:00 p.m., with 1.5 to 3 hr between successive messages ($M = 120$ min, $SD = .43$). On weekdays, messages were delivered during the "passing periods" between scheduled university courses to reduce burden and maximize compliance. Messages were delivered according to a fixed schedule that varied across days (e.g., the third message was delivered at 12:52 p.m. on Mondays and 12:16 p.m. on Tuesdays). Messages contained a link to a secure online survey. Subjects were instructed to respond within 30 min ($Mdn = 2$ min, $SD = 7$ min) and to refrain from responding at unsafe or inconvenient moments (e.g., while driving). During the baseline laboratory session, several procedures were used to promote compliance, including (a) delivering a test message to subjects' phones and confirming that they were able to successfully complete the online survey, (b) providing subjects with a 24/7 technical-support number, and (c) providing monetary bonuses for increased compliance.

EMA survey and data reduction. Current negative affect (afraid, nervous, worried, hopeless, sad) and positive affect (cheerful, content, enthusiastic, joy, relaxed, calm) at the moment of the survey prompt was rated using a 5-point scale (0, *not at all*, to 4, *extremely*). Stressor exposure was assessed using a binary item ("Did you experience one or more negative events in the past hour?"). A parallel item was used to assess recent positive events. A factor analysis (principal component extraction; oblimin rotation) of the negative- and positive-affect items yielded a two-factor solution, with robust loadings on the target scales (λs = .64–.88) and negligible cross-loadings (λs < |.19|). Both scales demonstrated adequate internal-consistency reliability at the between-subject (αs = .80–.88) and within-subject (αs = .92–93) levels. Within-subject reliability was evaluated using two-level unconditional models (items nested within subjects) implemented in *semTools* (Jorgensen et al., 2018) in *R*. The reliability of the Level 1 intercept represents McDonald's

w adjusted for differences between subjects (Nezlek, 2007; Raudenbush & Bryk, 2002). To better understand the nature of significant brain–EMA relations, we performed follow-up tests using composite anxiety (afraid, nervous, worried) and depression (hopeless, sad) facet scales (αs = .66–.79). EMA compliance was acceptable (*M* = 87.9%, *SD* = 6.1%, minimum = 71.4%, total assessments = 10,239).

Skin conductance modeling

Using standard MATLAB functions, we modeled skin conductance response data using an approach similar to that used for the fMRI data. A general linear model (GLM) was used to estimate skin conductance levels during the anticipatory epoch of each condition of the anxiety-provocation paradigm for each subject. Predictors from the first-level fMRI model (see below) were convolved with a canonical skin conductance response function, band-pass filtered to match the data, and *z*-transformed.

fMRI modeling and data reduction

Data exclusions. To assess residual global motion artifacts, we computed average volume-to-volume displacement for each scan using the motion-corrected data. Scans with excess artifacts (> 2 *SD*) were discarded. Subjects who lacked sufficient usable fMRI data (< 2 scans per task) or showed inadequate performance on the emotional-faces task (see above; accuracy < 2 *SD*) were excluded from analyses.

First-level fMRI models. Modeling was performed using *SPM12* (Version 6678; Wellcome Centre for Human Neuroimaging, 2022) and custom MATLAB scripts. Temporal band-pass filtering was set to the hemodynamic response function (HRF) and 128 s for low- and high-pass filtering, respectively. Regressors were convolved with a canonical HRF and temporal derivative. Nuisance variates included framewise displacement, motion parameters, cerebrospinal fluid time series, and instantaneous pulse and respiration. *ICA-AROMA* (Pruim et al., 2015) was used to extract other potential sources of noise (e.g., white-matter signal), and these were also included as nuisance variates. Volumes with framewise displacement greater than 0.5 mm were censored.

Anxiety provocation. A detailed description of the modeling procedure is available in Hur, Smith, et al. (2020). In brief, the *anxiety-provocation* task was modeled using variable-duration rectangular regressors time-locked to the anticipation epochs of threat or safety trials, to the presentation of aversive or benign stimulation, and

to rating trials (see Fig. S1). Volumes coincident with aversive stimulation were censored.

Threat-related faces. The faces task was modeled using fixed-duration rectangular regressors time-locked to the blocks of angry, fearful, or happy faces (see Fig. S2).

Brain metrics. To fuse the fMRI and EMA data streams, we functionally prescribed regions of interest (ROIs) at the group level on the basis of significant task effects in whole-brain voxelwise analyses (false discovery rate [FDR] *q* < .05, whole-brain corrected; see below) within anatomical regions selected on the basis of prior large-scale studies and meta-analyses (e.g., Chavanne & Robinson, 2021; Hur et al., 2018; Hur, Smith, et al., 2020). It merits comment that this is a conservative approach. This reflects the fact that task effects (Student's *t*) are estimated by dividing the mean within-subjects difference (e.g., threat vs. safety) by the between-subjects variation. All else being equal, regions showing stronger task effects will tend to evince less between-subject variance, constraining relations with external variables (e.g., momentary negative affect). For each region (e.g., MCC) and subject, regression coefficients were extracted and averaged across voxels using cubical masks centered on the local maxima identified in voxelwise analyses (Fig. 2). A faces-only ROI (seven voxels, 56 mm^3) was used for subcortical regions, whereas a larger faces, edges, and corners ROI (27 voxels, 216 mm^3) was used for cortical regions, consistent with prior fMRI-EMA research (e.g., Lopez et al., 2014). As a validity check, one-sample *t* tests were used to confirm the sign and magnitude of ROI-extracted values (not reported).

The goal of our study was to test the relevance of the threat-anticipation network identified in prior work to negative affect in the real world (Hur et al., 2020; Shackman & Fox, 2021). Accordingly, for the anxiety-provocation paradigm, analyses focused on activation during the anticipation of aversive compared with benign stimulation. Regression coefficients for the resulting threat-versus-safety contrast were extracted and averaged across voxels for the dorsal amygdala, BST, PAG, MCC, AI, FrO, and dlPFC. With the exception of the PAG—a small midline structure—coefficients were separately extracted for the left and right hemispheres. To minimize the number of comparisons and maximize statistical power, we used a factor analysis with principal component extraction and oblimin rotation to reduce data dimensionality. Here the ROI-level data served as manifest indicators of a theory-driven circuit of interest, and factor analysis provided a principled means of distinguishing relevant subcomponents or facets. Parallel analysis—which compares the eigenvalues of the sample correlation matrix with those
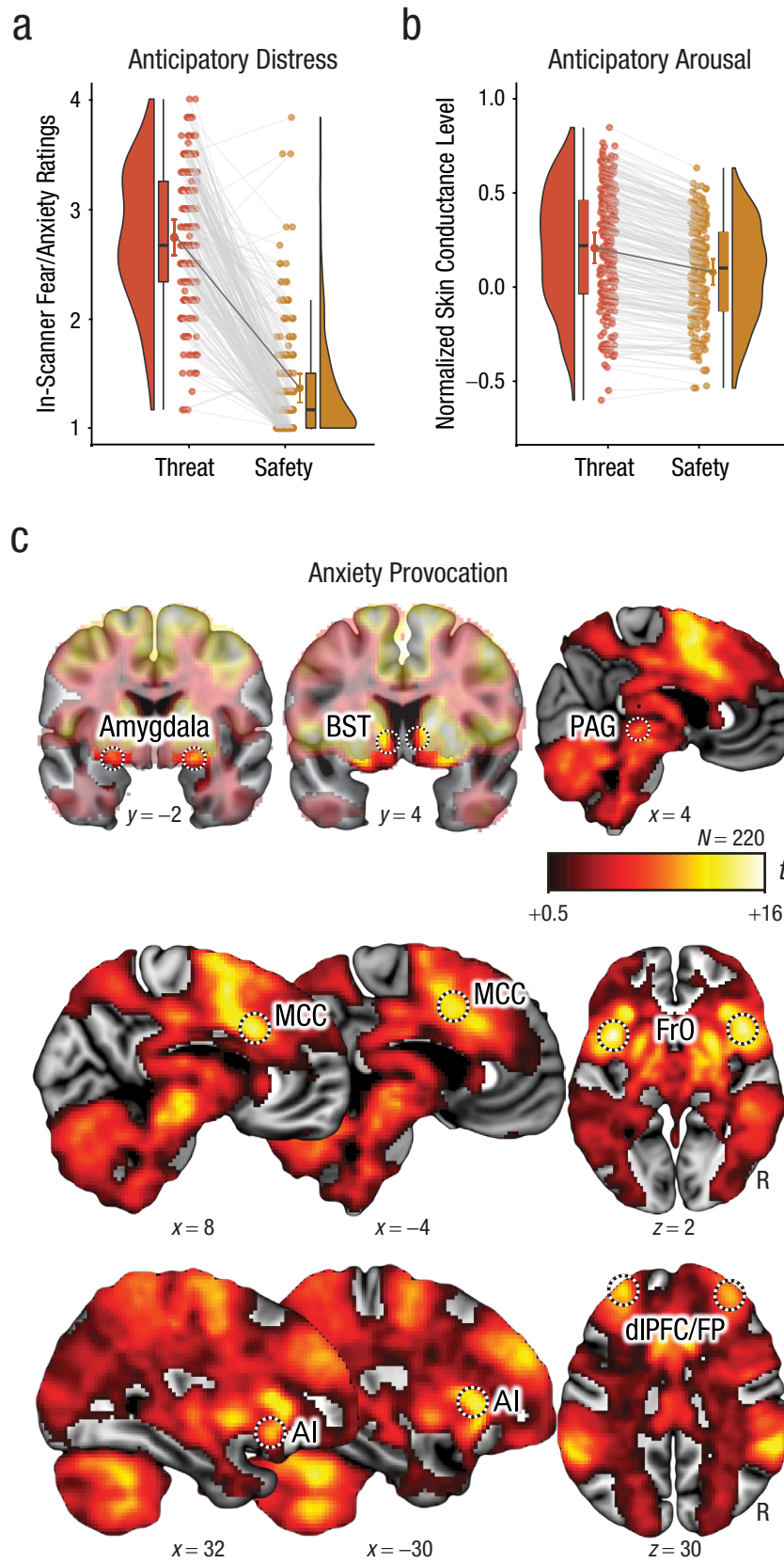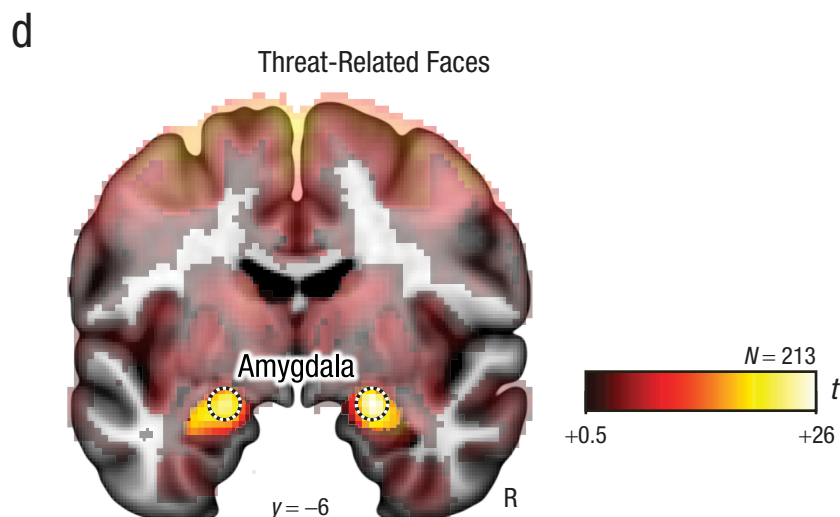
a

Anticipatory Distress

b

Anticipatory Arousal

c

Anxiety Provocation

Fig. 2. *(continued on next page)*

d

Threat-Related Faces

Amygdala

$N = 213$

t

+0.5   +26

$y = -6$ R

Fig. 2. Laboratory measures for the anxiety-provocation (threat-anticipation) and threat-related-faces paradigms. Mean in-scanner ratings of fear and anxiety (a) and normalized skin conductance level (b) are shown separately for the threat and safety conditions. Bean (i.e., half-violin) plots show the smoothed density distributions. Box-and-whisker plots indicate the medians (horizontal lines) and interquartile ranges (height of boxes); black whiskers depict 1.5 times the interquartile range. The adjacent colored dots connected by black lines indicate the condition means. Colored error bars indicate 95% confidence intervals for the means. Dots connected by gray lines depict the mean response for each subject and condition. Panel (c) depicts regions in which activation increased during the anxiety-provocation paradigm (threat > safety; false discovery rate [FDR] $q < .05$, whole-brain corrected). Panel (d) depicts regions in which activation increased during the threat-related-faces paradigm (threat-related faces > places; FDR $q < .05$, whole-brain corrected). The amygdala and bed nucleus of the stria terminalis (BST) images are masked to highlight suprathreshold voxels in the relevant regions. Black-and-white rings indicate the regions used for the integrative analyses of functional MRI (fMRI) and ecological momentary assessment (EMA; see the Method section and Tables S2 and S3 in the Supplemental Material for details). Coordinates are in Montreal Neurological Institute space. AI = anterior insula; dlPFC = dorsolateral prefrontal cortex; FP = frontal pole; FrO = frontal operculum; MCC = midcingulate cortex; PAG = periaqueductal gray; R = right.

obtained using random uncorrelated standardized normal variables—was used to determine the number of factors to retain. Parallel analysis was implemented using *nFactors* (Version 2.4.1; Raichle & Magis, 2020) for *R*. Visual inspection of the scree plot, the Kaiser criterion (eigenvalue > 1), and parallel analysis all indicated the presence of two factors, with frontocortical ROIs loading on the first factor and subcortical ROIs loading on the second (see Table S1 in the Supplemental Material). Similar results were yielded using varimax rotation (not reported). On the basis of this, we standardized (*z*-transformed) and averaged the ROI values to create composite measures of anxiety-related frontocortical ($\alpha = .89$) and subcortical ($\alpha = .82$) activity for each subject. Although this approach is widely used in the social and biological sciences— and has the advantage of reducing the neuroimaging data set from tens of thousands of voxels to two regional composites—it merits comment that the observed pattern of factor loadings necessarily reflects a combination of

biological and measurement differences (e.g., signal-to-noise) across regions. To clarify the unique contribution of specific regions (e.g., MCC), we performed follow-up tests using regional composites. Composites were created by averaging the standardized ROI values for the left and right hemispheres.

Threat-related faces. For the faces paradigm, analyses focused on dorsal amygdala reactivity to threat-related (i.e., fearful or angry) faces compared with places, consistent with prior work (e.g., Swartz et al., 2015). Mean coefficients were separately extracted for the left and right amygdalae, standardized, and averaged for each subject ($\alpha = .82$).

Hypothesis-testing strategy

Unless noted otherwise, hypothesis testing was performed using *SPSS* (Version 24.0.0.0). To guard against

error, a second analyst independently analyzed and confirmed key results.

In-scanner distress ratings and skin conductance.

To confirm the validity of the anxiety-provocation paradigm, we used repeated measures GLMs to test differences between threat and safety anticipation. Unfortunately, the sparse nature of the in-scanner ratings protocol (i.e., two ratings per valence per scan) precluded meaningful analyses of concurrent brain–behavior relations. Raincloud plots were generated using open-source code (Version 1.0.4; van Langen, 2020).

fMRI.

Standard whole-brain voxelwise GLMs with random effects were computed using *SPM12* and used to assess activation to the anxiety-provocation (threat-anticipation) and emotional-faces paradigms. Significance was assessed using FDR $q < .05$, whole-brain corrected. Some figures were created using *MRIcron* (Rorden, 2019) and *MRIcroGL* (Rorden, 2021). Clusters and local maxima were labeled using a combination of the Allen Institute, Harvard–Oxford, and Mai atlases (Desikan et al., 2006; Frazier et al., 2005; Hawrylycz et al., 2012; Mai et al., 2015; Makris et al., 2006) and a recently established consensus nomenclature (ten Donkelaar et al., 2018). Frontal operculum subdivisions were labeled using the nomenclature of Amunts (Amunts et al., 2010). Amygdala subdivisions were labeled using the atlases and recently developed ROIs (Tillman et al., 2018; Tyszka & Pauli, 2016).

Brain–EMA fusion.

As shown schematically in Figure 1, a series of HLMs—often termed multilevel or linear mixed models—was used to test relations between individual differences in task-related brain activity and moment-by-moment levels of *tonic* (stressor-independent) and *reactive* (stressor-dependent) negative affect, separately for each composite brain metric. HLM naturally handles the nested dependency and variable number of longitudinal assessments provided by each subject, unlike traditional repeated measures GLM approaches.

Here, the EMA-derived negative affect (continuous) and stressor (binary) time series (i.e., Level 1 variables) were nested within subjects (for details, see "EMA Survey and Data Reduction"). Intercepts were free to vary across subjects. Brain metrics were derived in the manner described above, were grand-mean centered, and served as continuous Level 2 predictors.

For hypothesis-testing purposes, a single HLM—incorporating terms for tonic and reactive negative affect—was implemented for each of the composite brain metrics. This has the advantage of providing estimates for each kind of affect (e.g., tonic) while controlling for the other (e.g., reactive). The following

equations outline the basic structure of the HLM in standard notation (Raudenbush & Bryk, 2002). At the first level, negative affect during EMA t for individual i was modeled as a function of stressor exposure; the absence of stressor exposure served as the reference category (i.e., baseline):

$$\text{negative affect}_{ti} = \pi_{0i} + \pi_{1i}(\text{stressor}) + e_{ti}. \quad (1a)$$

At the second level of the HLM, relations between stressors and negative affect were modeled as a function of individual differences of the focal brain metric:

$$\pi_{0i} = \beta_{00} + \beta_{01}(\text{brain}_i) + r_{0i} \quad (1b)$$

$$\pi_{1i} = \beta_{10} + \beta_{11}(\text{brain}_i) + r_{1i}. \quad (1c)$$

From a conceptual perspective, individual differences in reactive negative affect were estimated using a binary reference function (i.e., time series) indicating the self-reported presence or absence of stressor exposure at each EMA (Equation 1a). Individual differences in tonic negative affect were indexed by the intercept term in Equation 1a (i.e., each subject's average mood, controlling for stressor-dependent fluctuations).

HLMs were computed using the SPSS default covariance structure (variance components) and restricted maximum likelihood estimates. Standardized (z-transformed) variables were used for all analyses. For illustrative purposes, significant interactions are depicted for extreme values (±1 *SD*) of the relevant brain metric. The Šidák procedure was used to determine corrected two-tailed significance thresholds for family set of tests that encompassed multiple brain metrics derived from a single task (e.g., subcortical and frontocortical composites; Šidák, 1967).

Using the same general approach, we conducted follow-up analyses to determine whether significant brain–EMA associations generalize to positive affect and positive events, which would suggest a broader functional role. To gauge the added explanatory value (i.e., incremental validity) of significant brain metrics, we recomputed the relevant HLM after incorporating an alternative brain metric (e.g., amygdala reactivity to threat-related faces) or our multi-occasion index of trait negative emotionality, conceptually akin to performing a simultaneous multiple regression. Finally, to enhance interpretability, we decomposed significant brain–EMA associations by performing follow-up analyses for the anxious and depressed facets of negative affect and for the brain regions (e.g., MCC) included in the relevant composite. Conclusions remained unchanged when we

used square-root-transformed negative affect or controlled for variation in EMA compliance (not reported).

Results

We first confirmed that the anxiety-provocation and threat-related-faces paradigms had the intended effects on behavior and brain function. As expected, waiting to receive aversive stimulation was associated with robust increases in subjective symptoms of distress (in-scanner ratings of fear and anxiety), $t(219) = 29.42$, $p < .001$, and objective signs of arousal (skin conductance), $t(219) = 27.19$, $p < .001$ (Figs. 2a and 2b). As depicted in Figure 2c, and detailed in Table S2 in the Supplemental Material, voxelwise GLMs focused on the period of threat anticipation revealed significantly increased activity in key subcortical (dorsal amygdala, BST, PAG) and frontocortical (MCC, FrO, AI, and dlPFC extending into the frontal pole [FP]) regions of the threat-anticipation network (FDR $q < .05$, whole-brain corrected; Hur, Smith, et al., 2020; Shackman & Fox, 2021). Likewise, the presentation of threat-related faces was associated with increased activity in the dorsal amygdala (Fig. 2d), fusiform gyrus, and other regions of the ventral visual cortex (see Table S3 in the Supplemental Material).

To fuse the fMRI and EMA data streams, we first extracted measures of task-related activation (i.e., regression coefficients) from ROIs centered on peak voxels in key anatomical regions for each task and subject (black-and-white rings in Fig. 2; see Tables S2 and S3 for coordinates). To reduce the number of comparisons, we used a factor analysis to guide the construction of composite measures for the anxiety-provocation task. Results revealed two latent factors, with subcortical regions (dorsal amygdala, BST, and PAG) loading on one factor and frontocortical regions (MCC, AI, FrO, and dlPFC/frontal pole) loading on the other (see Table S1). On this basis, we standardized and averaged the ROI values to create composite measures of subcortical ($\alpha = .85$) and frontocortical ($\alpha = .89$) activation for each subject. A similar approach was used to create a bilateral amygdala composite for the threat-related-faces task ($\alpha = .82$). As shown schematically in Figure 1, a series of HLMs was then used to test relations between individual differences in task-related activation and momentary levels of tonic (stressor-independent) and reactive (stressor-dependent) negative affect. Unlike traditional repeated measures GLM approaches, HLM naturally handles the nested dependency and variable number of EMAs contributed by each subject.

We first examined the anxiety-provocation task. As shown in Figure 3a and Table 1, subcortical and frontocortical activation during threat anticipation was unrelated to tonic (stressor-independent) levels of negative affect (ps > .64). Outside the laboratory, stressor exposure was associated with a momentary increase in negative affect (ps < .001). Although subcortical activation during the threat-anticipation task was unrelated to the magnitude of this stressor-dependent distress ($p = .43$), frontocortical reactivity was significantly related ($\beta = -0.07$, $SE = 0.03$, $p = .02$) and remained significant after we applied a principled correction for the number of ROIs examined (Šidák $\alpha_{critical} = .025$). Closer inspection indicated that individuals who showed more activation in frontocortical regions when anticipating aversive stimulation experienced lower levels of negative affect in the moments following stressor exposure, consistent with a regulatory role (Fig. 3a, inset). This association remained significant ($\beta = -0.09$, $p = .03$) after analyses controlled for individual differences in subcortical reactivity, which were themselves not related to reactive distress ($p = .43$; see Table S4 in the Supplemental Material). Similar associations with frontocortical reactivity were evident for the anxious and depressed facets of momentary negative affect (βs = -0.07, ps = .04–.05; see Table S5 in the Supplemental Material). Follow-up tests indicated that frontocortical reactivity was unrelated to the frequency of momentary stressors ($r = -.01$, $p = .91$), and relations between frontocortical activation and reactive distress remained significant after analyses controlled for individual differences in the frequency of stressor exposure ($\beta = -0.07$, $p = .02$; see Table S6 in the Supplemental Material).

We next examined the emotional-faces task. Variation in amygdala reactivity to threat-related faces in the laboratory was unrelated to either tonic (stressor-independent) or reactive (stressor-dependent) levels of negative affect in the field (ps > .17; Fig. 3c and Table 1). Consistent with this null result, relations between frontocortical activation during the anxiety-provocation paradigm and reactive distress remained significant after analyses controlled for amygdala reactivity to threat-related faces, underscoring the unique explanatory contribution of frontocortical function ($\beta = -0.07$, $p = .03$; see Table S7 in the Supplemental Material).

Collectively, these results demonstrate that heightened frontocortical activation while waiting for aversive stimulation is associated with lower levels of negative affect during and following exposure to everyday stressors. This is consistent with either a narrow role in dampening distress or a broader role in regulating emotion. To address this ambiguity, we used HLM to perform a parallel analysis for positive affect and positive events. Results indicated that frontocortical activation was unrelated to either tonic or reactive positive affect, consistent with a narrower regulatory function (ps > .14; see Table S8 in the Supplemental Material).
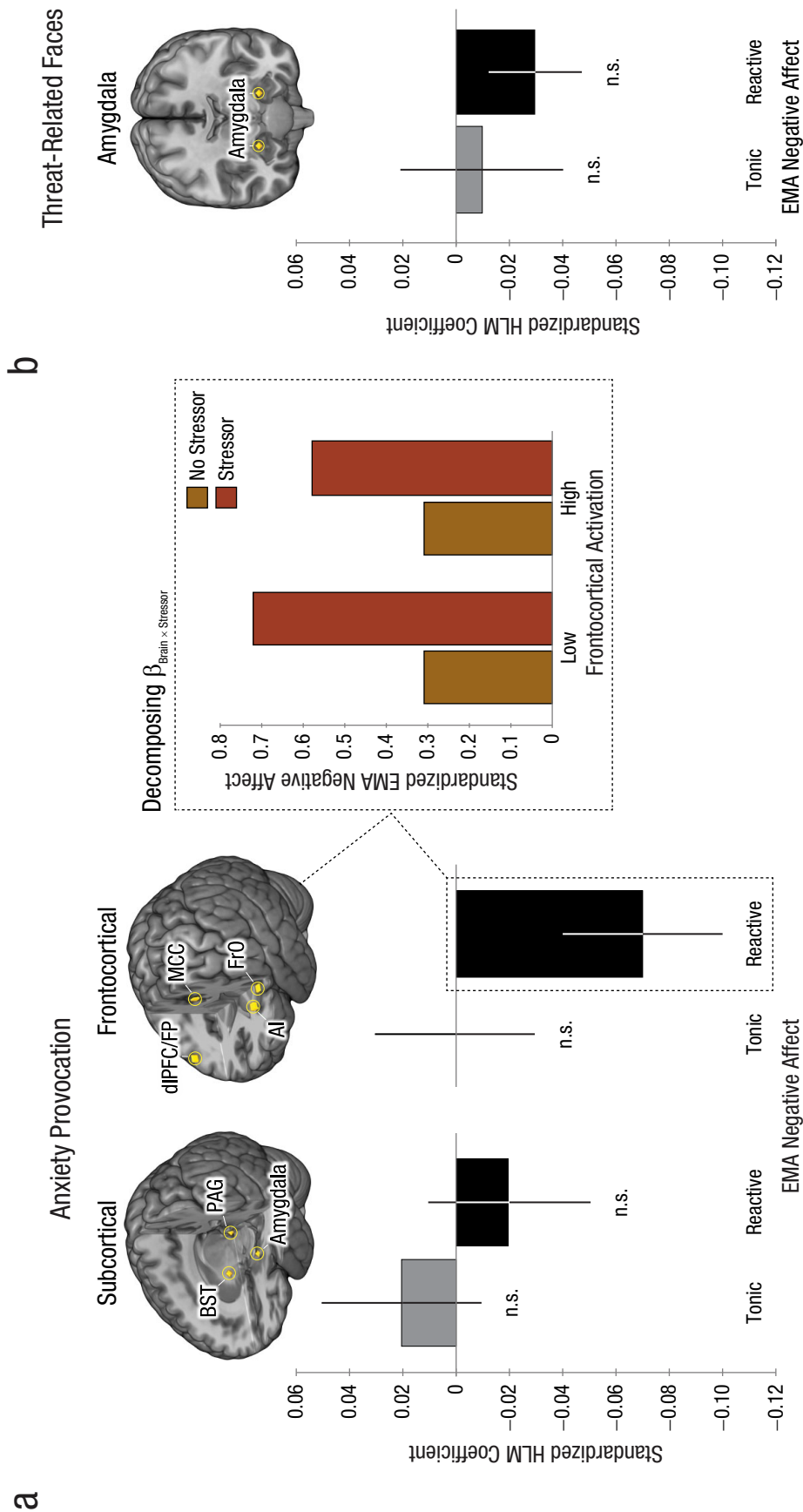
Fig. 3. Brain function in the laboratory and negative affect in the real world. Panel (a) depicts functional MRI (fMRI) and ecological momentary assessment (EMA) fusion results for the anxiety-provocation (threat anticipation) paradigm. The graphs on the left depict standardized hierarchical linear model (HLM) coefficients for EMA-derived measures of tonic (stressor-independent) negative affect in gray and reactive (stressor-dependent) negative affect in black, separately for the subcortical and frontocortical composites. Error bars indicate standard errors. The rendered brain images depict the regions contributing to each composite (gold). Some regions are not visible. The inset bar plot depicts the decomposition of the Brain × Stressor interaction for the frontocortical composite. For illustrative purposes, HLM-predicted levels of negative affect are depicted for assessments associated with the absence (orange) or presence (red) of recent real-world stressors, separately for extreme levels (low = −1 SD; high = +1 SD) of frontocortical activation. Hypothesis testing employed continuous measures. Panel (b) depicts the fMRI–EMA fusion results for the threat-related-faces paradigm. Conventions are identical to those in (a). AI = anterior insula; BST = bed nucleus of the stria terminalis; dlPFC = dorsolateral prefrontal cortex; FP = frontal pole; FrO = frontal operculum; MCC = midcingulate cortex; PAG = periaqueductal gray; n.s. = nonsignificant.

Table 1. Relations Between Laboratory Measures of Brain Function and Real-World Negative Affect

	Anxiety-provocation paradigm						Threat-related-faces paradigm		
	Subcortical composite			Frontocortical composite			Amygdala composite		
Factor	t	β	SE	t	β	SE	t	β	SE
Brain	0.47	0.02	0.03	0.00	0.00	0.03	−0.48	−0.01	0.03
Stressor (vs. absent)	14.93**	0.34	0.02	15.13**	0.34	0.02	14.85**	0.34	0.02
Brain × Stressor	−0.79	−0.02	0.03	−2.40*	−0.07	0.03	−1.36	−0.03	0.02

Note: The subcortical composite encompassed the bilateral dorsal amygdala, bilateral bed nucleus of the stria terminalis, and periaqueductal gray. The frontocortical composite encompassed the bilateral midcingulate cortex, frontal operculum, anterior insula, and dorsolateral prefrontal cortex/frontal pole. The brain-by-stressor term tested relations between neural function and reactive (stressor-dependent) negative affect. The same pattern of null results was evident in models that omitted the stressor and brain-by-stressor terms (not shown).
*$p \leq .05$. **$p < .001$.

In head-to-head comparisons of criterion validity, simple paper-and-pencil measures often outperform more sophisticated brain-imaging measures (Shackman & Fox, 2018). To clarify the explanatory value of frontocortical activation, we computed a new HLM that used a combination of frontocortical reactivity and a multi-scale, multi-occasion composite measure of trait negative emotionality (see the Method section) to explain momentary negative affect (which is conceptually akin to a multiple regression). As expected, negative emotionality promoted distress; individuals with a more negative temperament experienced higher levels of tonic and reactive negative affect in their daily lives ($ps < .001$), consistent with prior work (Bolger, 1990; Bolger & Schilling, 1991; Shackman et al., 2016; Thake & Zelenski, 2013). But more important, relations between frontocortical activation and reactive (stressor-dependent) negative affect remained significant after analyses controlled for differences in negative emotionality ($\beta = -0.06$, $p = .03$; see Table S9 in the Supplemental Material). In other words, frontocortical reactivity to the anxiety-provocation task accounted for variation in momentary distress above and beyond that explained by a traditional paper-and-pencil measure of emotional reactivity, underscoring the added explanatory value (incremental validity) of the neuroimaging metric.

Multiregion composites have a number of psychometric and statistical advantages but do not speak to the contributions of their constituent regions. To address this, we used a series of HLMs to decompose the frontocortical composite and determine the relevance of individual regions to momentary negative affect. As shown in Figure 4 and detailed in Table S10 in the Supplemental Material, individuals who showed greater activation in either the MCC or the FrO during the anxiety-provocation task experienced significantly lower levels of negative affect in the moments during and following stressor exposure in the field ($ps < .01$). Both regional associations remained significant after we corrected for the number of frontocortical ROIs examined (Šidák $\alpha_{\text{critical}} = .013$). None of the other frontocortical brain–EMA associations were significant ($ps > .11$). Follow-up tests indicated that relations between anxiety-related MCC activation and reactive negative affect remained significant after analyses controlled for variation in AI and dlPFC activation ($\beta = -0.08$, $p = .04$; Table S11 in the Supplemental Material). The same pattern was evident for the FrO ($\beta = -0.07$, $p = .05$; Table S12 in the Supplemental Material). AI and dlPFC were both unrelated to reactive negative affect in these models ($ps > .56$). Neither cingulo-opercular region was significantly related to reactive negative affect after analyses controlled for variation in the other (e.g., MCC controlling for FrO; $ps > .28$; Table S13 in the Supplemental Material), consistent with the substantial association between anxiety-related MCC and FrO activation ($r = .72$, $p < .001$). Taken together, these observations suggest that, among the frontocortical regions recruited by the anxiety-provocation paradigm, cingulo-opercular activation is most closely related to real-world variation in reactive (stressor-dependent) negative affect.

Our findings raise the possibility that the MCC and FrO represent a meaningful functional circuit. Consistent with this possibility, results from a series of supplementary analyses showed that these regions show robust coupling (intrinsic functional connectivity) at rest and are consistently coactivated across a range of experimental challenges (Laird et al., 2013; Yeo et al.,
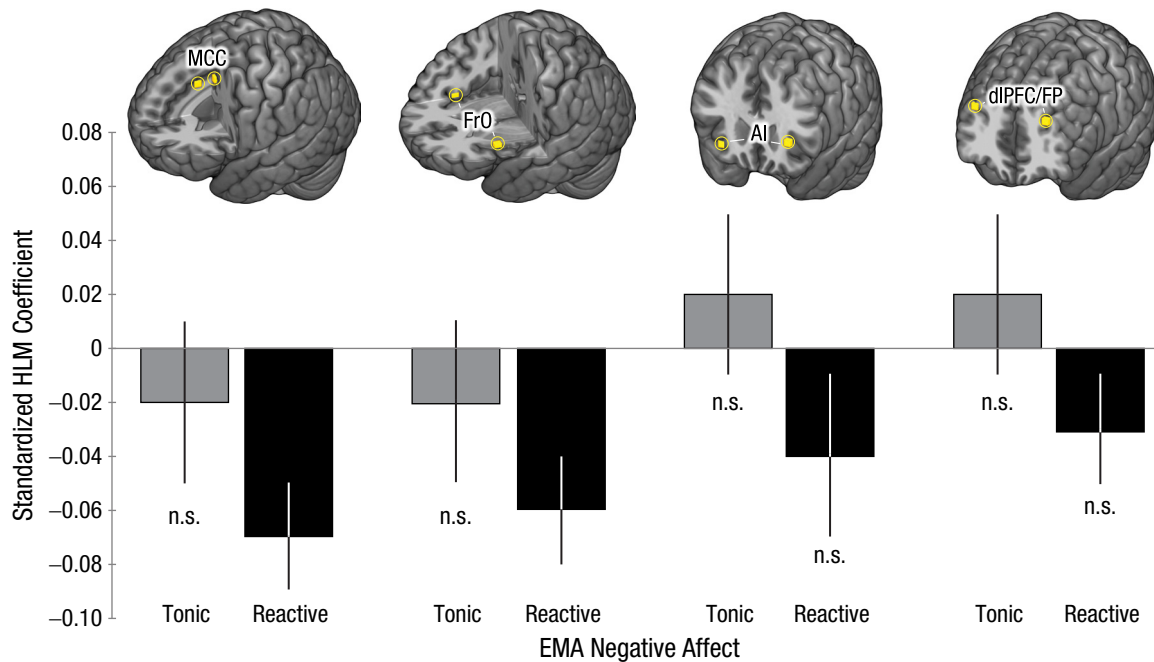
Fig. 4. Frontocortical function and real-world negative affect, indexed using ecological momentary assessment (EMA). The figure depicts the association between activation during the anxiety-provocation paradigm and momentary stressor reactivity, separately for the midcingulate cortex (MCC), frontal operculum (FrO), anterior insula (AI), and dorsolateral prefrontal cortex/frontal pole (dlPFC/FP). Data bars show standardized hierarchical linear model (HLM) coefficients for tonic (stressor-independent) negative affect in gray and reactive (stressor-dependent) negative affect in black. Error bars depict standard errors. n.s. = nonsignificant.

2011). These findings are described in more detail in the Supplemental Material and summarized in Figure S3 in the Supplemental Material.

Discussion

Anxiety, sadness, and other negative feelings are a hallmark of the human condition and play a central role in contemporary theories of decision-making, development, interpersonal processes, personality, psychopathology, and well-being (Fox et al., 2018). Recent work has begun to reveal the neural systems governing the expression and regulation of negative affect, but the relevance of these tantalizing laboratory discoveries to the real world has remained uncertain. Here, we used a combination of fMRI and EMA data to demonstrate that individuals who showed greater frontocortical activation during a well-established anxiety-provocation (threat-anticipation) task experience dampened reactive (stressor-dependent) distress in their daily lives (Fig. 3). Frontocortical activation was not significantly related to momentary positive affect or to tonic (stressor-independent) negative affect, suggesting a relatively narrow functional role. In a simultaneous HLM, frontocortical activation accounted for variation in daily distress above and beyond a conventional psychometric measure of trait negative emotionality, underscoring its added explanatory value. Follow-up analyses

indicated that, among the frontocortical regions that we examined in detail, this association predominantly reflected heightened engagement of a functionally coherent cingulo-opercular (MCC and FrO) circuit (Fig. 4 and Fig. S3).

These findings have implications for understanding the neural systems underlying negative affect. There is ample evidence that the MCC and FrO are recruited by distress-eliciting laboratory challenges, including instructed threat of shock, Pavlovian threat conditioning, and physical pain (Chavanne & Robinson, 2021; Fullana et al., 2016; Shackman et al., 2011; Xu et al., 2020). This has led some to conclude that the cingulo-opercular network plays a role in assembling and expressing negative affect (Etkin et al., 2015; Hinojosa et al., 2019; Milad & Quirk, 2012). Yet recent meta-analyses and large-sample imaging studies make it clear that the MCC and FrO are also recruited by tasks that demand controlled processing and behavioral flexibility, including popular assays of cognitive conflict (e.g., go/no-go) and emotion regulation (Langner et al., 2018; Morawetz et al., 2020; Shackman et al., 2011; Uddin, 2021). Furthermore, MCC activation tracks variation in both the cognitive demands associated with deliberate emotion regulation and the degree of regulatory success (Urry et al., 2009). These observations suggest that cingulo-opercular activation during aversive laboratory

challenges reflects spontaneous efforts to downregulate or inhibit distress, a process that some researchers have termed "implicit" emotion regulation (Shackman & Lapate, 2018). Our results—which demonstrate that heightened cingulo-opercular reactivity to an anxiety-provocation task is associated with lower levels of reactive (stressor-dependent) distress in daily life—are consistent with this hypothesis. While mechanistic evidence is scant, the present findings are aligned with work showing that surgical damage to the MCC (i.e., cingulotomy) is associated with increased emotional reactivity to painful stimuli in humans (Davis et al., 1994; Greenspan et al., 2008). Likewise, focal inactivation of the posterior MCC transiently increases defensive responses to intruder and snake threats in monkeys (Rahman et al., 2021). Together, this body of data is consistent with conceptual models that emphasize the importance of the cingulo-opercular network for flexibly controlling cognition, emotion, and action in situations in which automatic or habitual responses are inadequate, as when there is competition between plausible alternative actions or between action and inaction (e.g., passively responding to emotional challenges vs. deliberately regulating the response; Shackman et al., 2011; Uddin, 2021). The present results help to extend this framework from the artificial confines of the neuroimaging laboratory to the real world.

Clearly, important challenges remain. First, the present study was focused on understanding the relevance of anxiety-related brain function to momentary levels of negative affect in the daily lives of young adults. Moving forward, it will be useful to expand this to encompass nationally representative samples (LeWinn et al., 2017) and concurrent relations with trial-by-trial fluctuations in negative affect, an analytic approach not permitted by the sparse in-scanner ratings used here (Geuter et al., 2020; Lim et al., 2009). Second, our results indicate that subcortical reactivity to threat anticipation and amygdala reactivity to threat-related faces in the laboratory are unrelated to distress in the field, despite a relatively well-powered sample. Although there are a number of possible explanations, this null effect is not unprecedented. Three recent large-sample studies (Duke Neurogenetics Study: $N = 1,256$; Human Connectome Project: $N = 319$; Minnesota Twin Study: $N = 548$) failed to detect credible relations between amygdala reactivity to threat-related faces and individual differences in negative emotionality (MacDuffie et al., 2019; Silverman et al., 2019; West et al., 2021). Does this mean that the amygdala, BST, and PAG are unrelated to negative affect? No, mechanistic work in humans, monkeys, and rodents makes it abundantly clear that they are (Fox & Shackman, 2019; Hur et al., 2019). Instead, this work raises the possibility that

conventional fMRI measures of emotion perception (viewing photographs of fearful or angry faces) and generation (briefly waiting for aversive stimulation) are suboptimal probes of the aspects of subcortical function most relevant to everyday affect (i.e., "wrong" assay; Puccetti et al., 2021; Sicorello et al., 2021). Alternatively, it could be that isolated regional measures of subcortical function are only weakly predictive of conscious feelings of negative affect and, hence, to typical state, trait, and clinical assessments (Brown et al., 2019; Chang et al., 2015; Shackman & Fox, 2018). Adjudicating between these possibilities is a key challenge for future research.

Anxiety disorders and depression are defined, diagnosed, and treated on the basis of negative feelings experienced in the midst of daily life. These disorders impose a staggering burden on global public health, and existing treatments are far from curative for many patients, underscoring the urgency of developing a deeper understanding of the underlying neurobiology (Dieleman et al., 2020; Ormel et al., 2019; Sartori & Singewald, 2019; Vos et al., 2020). The present findings highlight the relevance of cingulo-opercular function for real-world distress. These observations lay the groundwork for the kinds of prospective-longitudinal and mechanistic studies that will be necessary to determine causation and develop more effective interventions. A relatively large sample and best-practice approaches to data acquisition, processing, and analysis enhance confidence in the robustness and translational relevance of these results.

Transparency

analyses. J. Hur, M. Kuhn, A. S. Fox, S. E. Grogans, and A. J. Shackman interpreted the data. S. E. Grogans, J. Hur, A. S. Fox, and A. J. Shackman wrote the manuscript. S. E. Grogans, M. Kuhn, J. Hur, and A. J. Shackman created the figures. M. Kuhn, J. Hur, and A. J. Shackman created the tables. A. J. Shackman supervised all aspects of the study. All authors contributed to reviewing and revising the manuscript and approved the final version for submission.

ORCID iD

Samiha Islam https://orcid.org/0000-0003-3238-7740

Acknowledgments

Supplemental Material

Additional supporting information can be found at http://journals.sagepub.com/doi/suppl/10.1177/09567976211056635

References

Amunts, K., Lenzen, M., Friederici, A. D., Schleicher, A., Morosan, P., Palomero-Gallagher, N., & Zilles, K. (2010). Broca's region: Novel organizational principles and multiple receptor mapping. *PLOS Biology*, *8*, Article e1000489. https://doi.org/10.1371/journal.pbio.1000489

Avants, B. B., Tustison, N. J., Song, G., Cook, P. A., Klein, A., & Gee, J. C. (2011). A reproducible evaluation of ANTs similarity metric performance in brain image registration. *NeuroImage*, *54*(3), 2033–2044.

Bach, D. R., & Friston, K. J. (2013). Model-based analysis of skin conductance responses: Towards causal models in psychophysiology. *Psychophysiology*, *50*, 15–22.

Biomedical Image Analysis Group. (2022). *IXI Dataset*. https://brain-development.org/ixi-dataset/

Bolger, N. (1990). Coping as a personality process: A prospective study. *Journal of Personality and Social Psychology*, *59*, 525–537.

Bolger, N., & Schilling, E. A. (1991). Personality and the problems of everyday life: The role of neuroticism in exposure and reactivity to daily stressors. *Journal of Personality*, *59*, 355–386.

Brown, R., Lau, H., & LeDoux, J. E. (2019). Understanding the higher-order approach to consciousness. *Trends in Cognitive Sciences*, *23*, 754–768.

Chang, L. J., Gianaros, P. J., Manuck, S. B., Krishnan, A., & Wager, T. D. (2015). A sensitive and specific neural signature for picture-induced negative affect. *PLOS Biology*, *13*, Article e1002180. https://doi.org/10.1371/journal.pbio.1002180

Chavanne, A. V., & Robinson, O. J. (2021). The overlapping neurobiology of adaptive and pathological anxiety: A meta-analysis of functional neural activation. *American Journal of Psychiatry*, *178*, 156–164.

Cox, R. W. (1996). AFNI: Software for analysis and visualization of functional magnetic resonance neuroimages. *Computers and Biomedical Research*, *29*, 162–173.

Davis, K. D., Hutchison, W. D., Lozano, A. M., & Dostrovsky, J. O. (1994). Altered pain and temperature perception following cingulotomy and capsulotomy in a patient with schizoaffective disorder. *Pain*, *59*, 189–199.

Desikan, R. S., Ségonne, F., Fischl, B., Quinn, B. T., Dickerson, B. C., Blacker, D., Buckner, R. L., Dale, A. M., Maguire, R. P., Hyman, B. T., Albert, M. S., & Killiany, R. J. (2006). An automated labeling system for subdividing the human cerebral cortex on MRI scans into gyral based regions of interest. *NeuroImage*, *31*, 968–980. https://doi.org/10.1016/j.neuroimage.2006.01.021

Dieleman, J. L., Cao, J., Chapin, A., Chen, C., Li, Z., Liu, A., Horst, C., Kaldjian, A., Matyasz, T., Woody Scott, K., Bui, A. L., Campbell, M., Duber, H. C., Dunn, A. C., Flaxman, A. D., Fitzmaurice, C., Naghavi, M., Sadat, N., Shieh, P., . . . Murray, C. J. L. (2020). US health care spending by payer and health condition, 1996-2016. *Journal of the American Medical Association*, *323*(9), 863–884.

Eskildsen, S. F., Coupé, P., Fonov, V., Manjón, J. V., Leung, K. K., Guizard, N., Wassef, S. N., Østergaard, L. R., Collins, D. L., & Alzheimer's Disease Neuroimaging Initiative. (2012). BEaST: Brain extraction based on nonlocal segmentation technique. *NeuroImage*, *59*, 2362–2373.

Etkin, A., Buchel, C., & Gross, J. J. (2015). The neural bases of emotion regulation. *Nature Reviews Neuroscience*, *16*, 693–700.

Faul, F., Erdfelder, E., Lang, A.-G., & Buchner, A. (2007). G*Power 3: A flexible statistical power analysis program for the social, behavioral, and biomedical sciences. *Behavior Research Methods*, *39*, 175–191.

First, M. B., Williams, J. B. W., Karg, R. S., & Spitzer, R. L. (2015). *Structured clinical interview for DSM-5—Research version (SCID-5 for DSM-5, research version; SCID-5-RV)*. American Psychiatric Association.

Fox, A. S., Lapate, R. C., Shackman, A. J., & Davidson, R. J. (2018). *The nature of emotion. Fundamental questions* (2nd ed.). Oxford University Press.

Fox, A. S., & Shackman, A. J. (2019). The central extended amygdala in fear and anxiety: Closing the gap between mechanistic and neuroimaging research. *Neuroscience Letters*, *693*, 58–67.

Frazier, J. A., Chiu, S., Breeze, J. L., Makris, N., Lange, N., Kennedy, D. N., Herbert, M. R., Bent, E. K., Koneru, V. K., Dieterich, M. E., Hodge, S. M., Rauch, S. L., Grant, P. E., Cohen, B. M., Seidman, L. J., Caviness, V. S., & Biederman, J. (2005). Structural brain magnetic resonance imaging of limbic and thalamic volumes in pediatric bipolar disorder. *American Journal of Psychiatry*, *162*, 1256–1265. https://doi.org/10.1176/appi.ajp.162.7.1256

Fullana, M. A., Harrison, B. J., Soriano-Mas, C., Vervliet, B., Cardoner, N., Àvila-Parcet, A., & Radua, J. (2016). Neural signatures of human fear conditioning: An updated and extended meta-analysis of fMRI studies. *Molecular Psychiatry*, *21*, 500–508.

Geuter, S., Reynolds Losin, E. A., Roy, M., Atlas, L. Y., Schmidt, L., Krishnan, A., Koban, L., Wager, T. D., & Lindquist, M. A. (2020). Multiple brain networks mediating stimulus–pain relationships in humans. *Cerebral Cortex*, *30*(7), 4204–4219. https://doi.org/10.1093/cercor/bhaa048

Goldberg, L. R., Johnson, J. A., Eber, H. W., Hogan, R., Ashton, M. C., Cloninger, C. R., & Gough, H. C. (2006). The International Personality Item Pool and the future of public-domain personality measures. *Journal of Research in Personality*, *40*, 84–96.

Grabner, G., Janke, A. L., Budge, M. M., Smith, D., Pruessner, J., & Collins, D. L. (2006). Symmetric atlasing and model based segmentation: An application to the hippocampus in older adults. In R. Larsen, M. Nielsen, & J. Sporring (Eds.) *Medical Image Computing and Computer-Assisted Intervention – MICCAI 2006. Lecture Notes in Computer Science* (Vol. 4191, pp. 58–66). Springer. https://doi.org/10.1007/11866763_8

Greenspan, J. D., Coghill, R. C., Gilron, I., Sarlani, E., Veldhuijzen, D. S., & Lenz, F. A. (2008). Quantitative somatic sensory testing and functional imaging of the response to painful stimuli before and after cingulotomy for obsessive-compulsive disorder (OCD). *European Journal of Pain*, *12*, 990–999.

Greve, D. N., & Fischl, B. (2009). Accurate and robust brain image alignment using boundary-based registration. *NeuroImage*, *48*, 63–72.

Hauner, K. K., Zinbarg, R. E., & Revelle, W. (2014). A latent variable model approach to estimating systematic bias in the oversampling method. *Behavior Research Methods*, *46*, 786–797.

Hawrylycz, M. J., Lein, E. S., Guillozet-Bongaarts, A. L., Shen, E. H., Ng, L., Miller, J. A., van de Lagemaat, L. N., Smith, K. A., Ebbert, A., Riley, Z. L., Abajian, C., Beckmann, C. F., Bernard, A., Bertagnolli, D., Boe, A. F., Cartagena, P. M., Chakravarty, M. M., Chapin, M., Chong, J., . . . Jones, A. R. (2012). An anatomically comprehensive atlas of the adult human brain transcriptome. *Nature*, *489*, 391–399.

Hinojosa, C. A., Kaur, N., VanElzakker, M. B., & Shin, L. M. (2019). Cingulate subregions in posttraumatic stress disorder, chronic stress, and treatment. In B. A. Vogt (Ed.), *Handbook of clinical neurology* (Vol. 166, pp. 355–370). Elsevier.

Hofmann, W., & Patel, P. V. (2015). SurveySignal: A convenient solution for experience sampling research using participants' own smartphones. *Social Science Computer Review*, *33*, 235–253. https://doi.org/10.1177/0894439314525117

Hur, J., DeYoung, K. A., Islam, S., Anderson, A. S., Barstead, M. G., & Shackman, A. J. (2020). Social context and the real-world consequences of social anxiety. *Psychological Medicine*, *50*, 1989–2000.

Hur, J., Kaplan, C. M., Smith, J. F., Bradford, D. E., Fox, A. S., Curtin, J. J., & Shackman, A. J. (2018). Acute alcohol administration dampens central extended amygdala reactivity. *Scientific Reports*, *8*, Article 16702. https://doi.org/10.1038/s41598-018-34987-3

Hur, J., Smith, J. F., DeYoung, K. A., Anderson, A. S., Kuang, J., Kim, H. C., Tillman, R. M., Kuhn, M., Fox, A. S., & Shackman, A. J. (2020). Anxiety and the neurobiology of temporally uncertain threat anticipation. *The Journal of Neuroscience*, *40*, 7949–7964.

Hur, J., Stockbridge, M. D., Fox, A. S., & Shackman, A. J. (2019). Dispositional negativity, cognition, and anxiety disorders: An integrative translational neuroscience framework. *Progress in Brain Research*, *247*, 375–436.

Jenkinson, M., Beckmann, C. F., Behrens, T. E., Woolrich, M. W., & Smith, S. M. (2012). FSL. *Neuroimage*, *62*(2), 782–790.

John, O. P., Naumann, L. P., & Soto, C. J. (2008). Paradigm shift to the integrative big-five trait taxonomy: History, measurement, and conceptual issues. In O. P. John, R. W. Robins, & L. A. Pervin (Eds.), *Handbook of personality: Theory and research* (pp. 114–158). Guilford Press.

Jorgensen, T. D., Pornprasertmanit, S., Schoemann, A. M., & Rosseel, Y. (2018). *semTools: Useful tools for structural equation modeling* (R Package Version 0.5-1) [Computer software]. https://CRAN.R-project.org/package=semTools

Kenwood, M. M., & Kalin, N. H. (2021). Nonhuman primate models to explore mechanisms underlying early-life temperamental anxiety. *Biological Psychiatry*, *89*, 659–671.

Laird, A. R., Eickhoff, S. B., Rottschy, C., Bzdok, D., Ray, K. L., & Fox, P. T. (2013). Networks of task co-activations. *NeuroImage*, *80*, 505–514.

Langner, R., Leiberg, S., Hoffstaedter, F., & Eickhoff, S. B. (2018). Towards a human self-regulation system: Common and distinct neural signatures of emotional and behavioural control. *Neuroscience & Biobehavioral Reviews*, *90*, 400–410.

LeWinn, K. Z., Sheridan, M. A., Keyes, K. M., Hamilton, A., & McLaughlin, K. A. (2017). Sample composition alters

associations between age and brain structure. *Nature Communications*, *8*, Article 874. https://doi.org/10.1038/s41467-017-00908-7

Lim, S. L., Padmala, S., & Pessoa, L. (2009). Segregating the significant from the mundane on a moment-to-moment basis via direct and indirect amygdala contributions. *Proceedings of the National Academy of Sciences, USA*, *106*, 16841–16846.

Lopez, R. B., Hofmann, W., Wagner, D. D., Kelley, W. M., & Heatherton, T. F. (2014). Neural predictors of giving in to temptation in daily life. *Psychological Science*, *25*(7), 1337–1344. https://doi.org/10.1177%2F0956797614531492

Lorio, S., Fresard, S., Adaszewski, S., Kherif, F., Chowdhury, R., Frackowiak, R. S., Ashburner, J., Helms, G., Weiskopf, N., Lutti, A., & Draganski, B. (2016). New tissue priors for improved automated classification of subcortical brain structures on MRI. *Neuroimage*, *130*, 157–166.

MacDuffie, K. E., Knodt, A. R., Radtke, S. R., Strauman, T. J., & Hariri, A. R. (2019). Self-rated amygdala activity: An auto-biological index of affective distress. *Personality Neuroscience*, *2*, Article e1. https://doi.org/10.1017/pen.2019.1

Mai, J. K., Majtanik, M., & Paxinos, G. (2015). *Atlas of the human brain* (4th ed.). Academic Press.

Makris, N., Goldstein, J. M., Kennedy, D., Hodge, S. M., Caviness, V. S., Faraone, S. V., Tsuang, M. T., & Seidman, L. J. (2006). Decreased volume of left and total anterior insular lobule in schizophrenia. *Schizophrenia Research*, *83*, 155–171.

McCormick, M., Liu, X., Jomier, J., Marion, C., & Ibanez, L. (2014). ITK: Enabling reproducible research and open science. *Frontiers in Neuroinformatics*, *8*, Article 13. https://doi.org/10.3389/fninf.2014.00013

Milad, M. R., & Quirk, G. J. (2012). Fear extinction as a model for translational neuroscience: Ten years of progress. *Annual Review of Psychology*, *63*, 129–151.

Miller, K. L., Alfaro-Almagro, F., Bangerter, N. K., Thomas, D. L., Yacoub, E., Xu, J., Bartsch, A. J., Jbabdi, S., Sotiropoulos, S. N., Andersson, J. L., Griffanti, L., Douaud, G., Okell, T. W., Weale, P., Dragonu, I., Garratt, S., Hudson, S., Collins, R., Jenkinson, M., Matthews, P. M., & Smith, S. M. (2016). Multimodal population brain imaging in the UK Biobank prospective epidemiological study. *Nature Neuroscience*, *19*, 1523–1536.

Mobbs, D., Adolphs, R., Fanselow, M. S., Barrett, L. F., LeDoux, J. E., Ressler, K., & Tye, K. M. (2019). Viewpoints: Approaches to defining and investigating fear. *Nature Neuroscience*, *22*, 1205–1216.

Morawetz, C., Riedel, M. C., Salo, T., Berboth, S., Eickhoff, S. B., Laird, A. R., & Kohn, N. (2020). Multiple large-scale neural networks underlying emotion regulation. *Neuroscience & Biobehavioral Reviews*, *116*, 382–395.

The National Academies of Sciences, Engineering, and Medicine. (2021). *Mental health, substance use, and well-being in higher education: Supporting the whole student*. The National Academies Press.

Nezlek, J. B. (2007). A multilevel framework for understanding relationships among traits, states, situations and behaviours. *European Journal of Personality*, *21*, 789–810.

Ormel, J., Kessler, R. C., & Schoevers, R. (2019). Depression: More treatment but no drop in prevalence: How effective is treatment? And can we do better? *Current Opinion in Psychiatry*, *32*, 348–354.

Pruim, R. H. R., Mennes, M., van Rooij, D., Llera, A., Buitelaar, J. K., & Beckmann, C. F. (2015). ICA-AROMA: A robust ICA-based strategy for removing motion artifacts from fMRI data. *NeuroImage*, *112*, 267–277.

Puccetti, N. A., Schaefer, S. M., van Reekum, C. M., Ong, A. D., Almeida, D. M., Ryff, C. D., Davidson, R. J., & Heller, A. S. (2021). Linking amygdala persistence to real-world emotional experience and psychological well-being. *The Journal of Neuroscience*, *41*, 3721–3730.

Rahman, S. S., Mulvihill, K., Wood, C. M., Quah, S. K. L., Horst, N. K., Clarke, H. F., Cockcroft, G. J., Santangelo, A. M., & Roberts, A. C. (2021). Differential contribution of anterior and posterior midcingulate subregions to distal and proximal threat reactivity in marmosets. *Cerebral Cortex*, *31*(10), 4765–4780.

Raichle, G., & Magis, D. (2020, March 28, 2020). *nFactors: Parallel analysis and other graphical solutions to the Cattell scree test* (Version 2.4.1) [Computer software]. https://cran.r-project.org/web/packages/nFactors/index.html

Raudenbush, S. W., & Bryk, A. S. (2002). *Hierarchical linear models: Applications and data analysis methods* (2nd ed.). SAGE.

Rorden, C. (2019, September 2, 2019). *MRIcron* [Computer software]. https://www.nitrc.org/projects/mricron

Rorden, C. (2021, October 6, 2021). *MRIcroGL* [Computer software]. https://www.nitrc.org/projects/mricrogl

Sartori, S. B., & Singewald, N. (2019). Novel pharmacological targets in drug development for the treatment of anxiety and anxiety-related disorders. *Pharmacology & Therapeutics*, *204*, Article 107402. https://doi.org/10.1016/j.pharmthera.2019.107402

Schönbrodt, F. D., & Perugini, M. (2013). At what sample size do correlations stabilize? *Journal of Research in Personality*, *47*, 609–612.

Shackman, A. J., & Fox, A. S. (2018). Getting serious about variation: Lessons for clinical neuroscience. *Trends in Cognitive Sciences*, *22*, 368–369.

Shackman, A. J., & Fox, A. S. (2021). Two decades of anxiety neuroimaging research: New insights and a look to the future. *American Journal of Psychiatry*, *178*, 106–109.

Shackman, A. J., & Lapate, R. C. (2018). How are emotions regulated by context and cognition? In A. S. Fox, R. C. Lapate, A. J. Shackman, & R. J. Davidson (Eds.), *The nature of emotion: Fundamental questions* (2nd ed., pp. 177–179). Oxford University Press.

Shackman, A. J., Salomons, T. V., Slagter, H. A., Fox, A. S., Winter, J. J., & Davidson, R. J. (2011). The integration of negative affect, pain and cognitive control in the cingulate cortex. *Nature Reviews Neuroscience*, *12*, 154–167.

Shackman, A. J., Tromp, D. P. M., Stockbridge, M. D., Kaplan, C. M., Tillman, R. M., & Fox, A. S. (2016). Dispositional negativity: An integrative psychological and neurobiological perspective. *Psychological Bulletin*, *142*, 1275–1314.

Shackman, A. J., Weinstein, J. S., Hudja, S. N., Bloomer, C. D., Barstead, M. G., Fox, A. S., & Lemay, E. P., Jr. (2018).

Dispositional negativity in the wild: Social environment governs momentary emotional experience. *Emotion*, *18*, 707–724.

Sicorello, M., Herzog, J., Wager, T. D., Ende, G., Müller-Engelmann, M., Herpertz, S. C., Bohus, M., Schmahl, C., Paret, C., & Niedtfeld, I. (2021). Affective neural signatures do not distinguish women with emotion dysregulation from healthy controls: A mega-analysis across three task-based fMRI studies. *NeuroImage: Reports*, *1*(2), Article 100019. https://doi.org/10.1101/2021.02.03.21251077

Šidák, Z. (1967). Rectangular confidence regions for the means of multivariate normal distributions. *Journal of the American Statistical Association*, *62*, 626–633.

Silverman, M. H., Wilson, S., Ramsay, I. S., Hunt, R. H., Thomas, K. M., Krueger, R. F., & Iacono, W. G. (2019). Trait neuroticism and emotion neurocircuitry: Functional magnetic resonance imaging evidence for a failure in emotion regulation. *Development and Psychopathology*, *31*, 1085–1099.

Swartz, J. R., Knodt, A. R., Radtke, S. R., & Hariri, A. R. (2015). A neural biomarker of psychological vulnerability to future life stress. *Neuron*, *85*, 505–511.

ten Donkelaar, H. J., Tzourio-Mazoyer, N., & Mai, J. K. (2018). Toward a common terminology for the gyri and sulci of the human cerebral cortex. *Frontiers in Neuroanatomy*, *12*, Article 93. https://doi.org/10.3389/fnana.2018.00093

Thake, J., & Zelenski, J. M. (2013). Neuroticism, BIS, and reactivity to discrete negative mood inductions. *Personality and Individual Differences*, *54*, 208–213.

Tillman, R. M., Stockbridge, M. D., Nacewicz, B. M., Torrisi, S., Fox, A. S., Smith, J. F., & Shackman, A. J. (2018). Intrinsic functional connectivity of the central extended amygdala. *Human Brain Mapping*, *39*, 1291–1312.

Tustison, N. J., Avants, B. B., Cook, P. A., Zheng, Y. J., Egan, A., Yushkevich, P. A., & Gee, J. C. (2010). N4ITK: Improved N3 bias correction. *IEEE Transactions on Medical Imaging*, *29*, 1310–1320.

Tyszka, J. M., & Pauli, W. M. (2016). In vivo delineation of subdivisions of the human amygdaloid complex in a high-resolution group template. *Human Brain Mapping*, *37*, 3979–3998.

Uddin, L. Q. (2021). Cognitive and behavioural flexibility: Neural mechanisms and clinical considerations. *Nature Reviews Neuroscience*, *22*, 167–179. https://doi.org/10.1038/s41583-021-00428-w

Urry, H. L., van Reekum, C. M., Johnstone, T., & Davidson, R. J. (2009). Individual differences in some (but not all) medial prefrontal regions reflect cognitive demand while regulating unpleasant emotion. *NeuroImage*, *47*, 852–863.

van Langen, J. (2020). *Open-visualizations in R and Python*. Zenodo. https://doi.org/10.5281/zenodo.3715576

Vos, T., Lim, S. S., Abbafati, C., Abbas, K. M., Abbasi, M., Abbasifard, M., Abbasi-Kangevari, M., Abbastabar, H., Abd-Allah, F., Abdelalim, A., Abdollahi, M., Abdollahpour, I., Abolhassani, H., Aboyans, V., Abrams, E. M., Abreu, L. G., Abrigo, M. R. M., Abu-Raddad, L. J., Abushouk, A. I., . . . Murray, C. J. L. (2020). Global burden of 369 diseases and injuries in 204 countries and territories, 1990–2019: A systematic analysis for the Global Burden of Disease Study 2019. *The Lancet*, *396*(10258), 1204–1222.

Wellcome Centre for Human Neuroimaging. (2022). *SPM* (Version 6678) [Computer software]. https://fil.ion.ucl.ac.uk/spm/

West, H. V., Burgess, G. C., Dust, J., Kandala, S., & Barch, D. M. (2021). Amygdala activation in cognitive task fMRI varies with individual differences in cognitive traits. *Cognitive, Affective, & Behavioral Neuroscience*, *21*(1), 254–264. https://doi.org/10.3758/s13415-021-00863-3

Xu, A., Larsen, B., Baller, E. B., Scott, J. C., Sharma, V., Adebimpe, A., Basbaum, A. I., Dworkin, R. H., Edwards, R. R., Woolf, C. J., Eickhoff, S. B., Eickhoff, C. R., & Satterthwaite, T. D. (2020). Convergent neural representations of experimentally-induced acute pain in healthy volunteers: A large-scale fMRI meta-analysis. *Neuroscience & Biobehavioral Reviews*, *112*, 300–323.

Yeo, B. T., Krienen, F. M., Sepulcre, J., Sabuncu, M. R., Lashkari, D., Hollinshead, M., Roffman, J. L., Smoller, J. W., Zöllei, L., Polimeni, J. R., Fischl, B., Liu, H., & Buckner, R. L. (2011). The organization of the human cerebral cortex estimated by intrinsic functional connectivity. *Journal of Neurophysiology*, *106*, 1125–1165.

Supplementary Method and Results

Juyoen Hur[1]*
Manuel Kuhn[2]*
Shannon E. Grogans[3]*
Allegra S. Anderson[6]
Samiha Islam[7]
Hyung Cho Kim[3,4]
Rachael M. Tillman[3]
Andrew S. Fox[8,9]
Jason F. Smith[3]†
Kathryn A. DeYoung[3]†
Alexander J. Shackman[3,4,5]†

[1]Department of Psychology, Yonsei University, Seoul 03722, Republic of Korea. [2]Center for Depression, Anxiety and Stress Research, McLean Hospital, Harvard Medical School, Belmont, MA 02478 USA. Department of [3]Psychology; [4]Neuroscience and Cognitive Science Program; and [5]Maryland Neuroimaging Center, University of Maryland, College Park, MD 20742 USA. [6]Department of Psychological Sciences, Vanderbilt University, Nashville, TN 37240 USA. [7]Department of Psychology, University of Pennsylvania, Philadelphia, PA USA. [8]Department of Psychology and [9]California National Primate Research Center, University of California, Davis, CA 95616 USA

* contributed equally * | † contributed equally

Address Correspondence to:
Juyoen Hur (jhur1@yonsei.ac.kr) or Alexander J. Shackman (shackman@umd.edu)

Table of Contents

Detailed Acknowledgements

Detailed Author Contributions

A.J.S., K.A.D., and J.F.S. designed the overall study. J.F.S. and A.J.S. developed and optimized the imaging paradigm. K.A.D. and A.J.S. developed and optimized the EMA paradigm. K.A.D. managed data collection and study administration. K.A.D., J.F.S., A.S.A, S.I., and R.M.T. collected data. K.A.D. and J.H. processed and analyzed EMA data. J.F.S. and M.K. developed data processing and analytic software for imaging analyses. J.H., J.F.S., H.C.K., and R.M.T. processed imaging data. J.H., M.K., J.F.S., and A.J.S. developed the strategy for the imaging analyses. M.K., J.H., and J.F.S. analyzed imaging data. J.H. and A.J.S. developed the strategy for the EMA-imaging analyses. J.H., M.K., A.S.F., S.E.G., and A.J.S. interpreted data. S.E.G., J.H., A.S.F., and A.J.S. wrote the paper. S.E.G., M.K., J.H., and A.J.S. created figures. M.K., J.H., and A.J.S. created tables. A.J.S. funded and supervised all aspects of the study. All authors contributed to reviewing and revising the paper and approved the final version.

Continued…
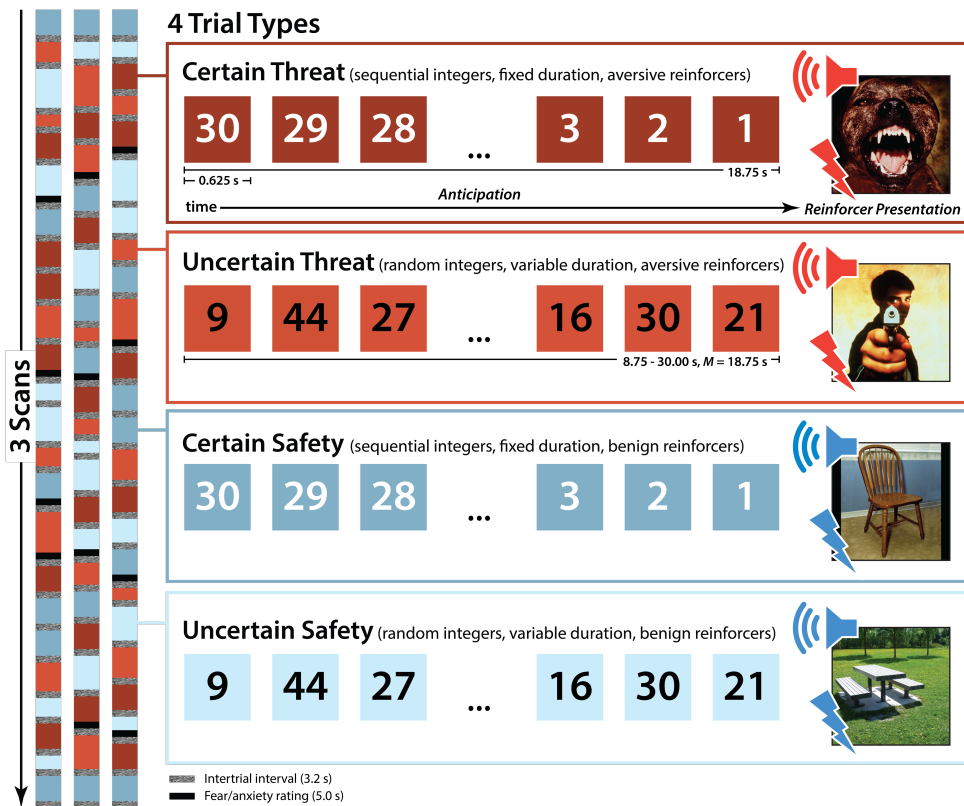
Supplementary Figure S1. **Anxiety-Provocation Paradigm.** The anxiety-provocation (threat-anticipation) task took the form of a 2 (*Valence:* Threat/Safety) × 2 (*Temporal Certainty:* Certain/Uncertain) randomized event-related design, as described in detail elsewhere (Hur et al., 2020). Subjects were completely informed about the task design and contingencies prior to scanning. The task was administered in 3 scans, with short breaks between scans. On Certain-Threat trials, subjects saw a descending stream of integers ('count-down;' e.g. 30, 29, 28...3, 2, 1) for 18.75 s. To ensure robust anxiety, this anticipation epoch always culminated with the delivery of a noxious electric shock, unpleasant photographic image (e.g., mutilated body), and thematically related audio clip (e.g., scream, gunshot). Uncertain-Threat trials were similar, but the integer stream was randomized and presented for an uncertain and variable duration (8.75-30.00 s; *M*=18.75 s). Subjects knew that something aversive was going to occur, but they had no way of knowing precisely *when*. The mean duration of the anticipation epoch was chosen to enhance detection of task-related differences in the blood oxygen level-dependent (BOLD) signal (Henson, 2007a), and was identical across trial types, ensuring an equal number of measurements. Safety trials were similar, but terminated with the delivery of benign reinforcers (e.g., just-perceptible electrical stimulation and neutral audiovisual stimuli). Valence was continuously signaled during the anticipation epoch by the background color of the display. White-noise visual masks (3.2 s) were presented between trials to minimize persistence of visual reinforcers in iconic memory. Subjects were periodically prompted to rate the intensity of negative affect ('fear/anxiety') experienced a few seconds earlier, during the *anticipation* period of the prior trial. Each condition was rated twice per scan. Skin conductance was continuously acquired. ***Design Consideration.*** The major aim of the present study was to understand the relevance of anxiety-related brain function to negative affect as it is experienced in the midst of everyday life. Prior work using this paradigm demonstrates that both kinds of threat anticipation—certain and uncertain—produce similar increases in anxious distress and arousal and recruit highly overlapping brain circuits (Hur et al., 2020). Therefore, the present analyses focused on the overall effect of threat anticipation—aggregated across the certainty manipulation—as detailed in the main report.
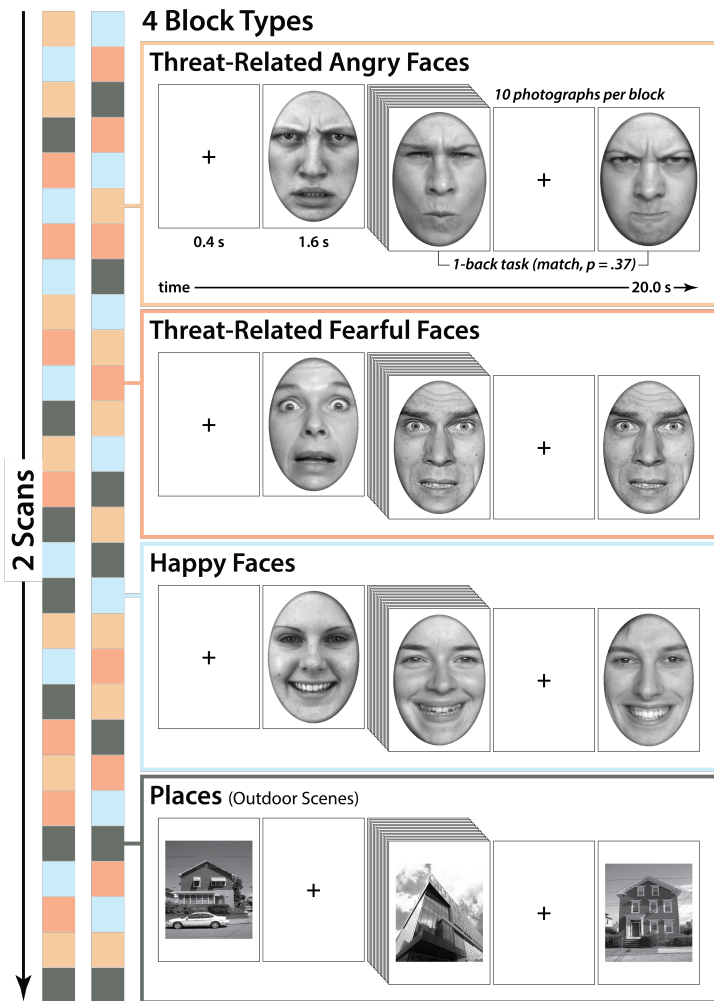
Supplementary Figure S2. **Emotional Faces Paradigm**. The faces task took the form of a pseudo-randomized block design and was administered in 2 scans, with a short break between scans. During each scan, subjects viewed photographs of adult models (half female) depicting angry faces, fearful faces, happy faces, or places (7 blocks/condition/scan). To maximize signal strength and homogeneity, and minimize potential habituation (Henson, 2007b; Maus, van Breukelen, Goebel, & Berger, 2010; Plichta et al., 2014), blocks consisted of 10 photographs (1.6 s) separated by fixation crosses (0.4 s). To ensure engagement, subjects judged whether the current photograph matched that presented on the prior trial (i.e., a '1-back' continuous performance task). Matches occurred 37.1% of the time. To minimize potential habituation, each photograph was presented once or twice. Face stimuli were adapted from prior work (Gamer, Schmitz, Tittgemeyer, & Schilbach, 2013; Scheller, Büchel, & Gamer, 2012) and included photographs of prototypical emotional expressions from Ekman and Friesen's Pictures of Facial Affect (Ekman & Friesen, 1976), the FACES database (Ebner, Riediger, & Lindenberger, 2010), the Karolinska Directed Emotional Faces database (http://www.emotionlab.se/resources/kdef), and the NimStim Face Stimulus Set (https://www.macbrain.org/resources.htm). Color photographs were converted to grayscale, brightness normalized, and masked to occlude non-facial features. Place stimuli consisted of grayscale photographs of outdoor scenes focused on single-family residential buildings ('houses') or urban commercial buildings ('skyscrapers'), and were also adapted from prior work (Choi, Padmala, & Pessoa, 2012, 2015).

Table S1. Oblimin-rotated factor loadings for anxiety-provocation (threat-anticipation) regions of interest.

Region of Interest	Frontocortical Factor	Subcortical Factor
R Dorsolateral Prefrontal Cortex / Frontal Pole	**0.88**	-0.22
L Frontal Operculum	**0.82**	0.05
L Midcingulate Cortex	**0.80**	0.05
L Dorsolateral Prefrontal Cortex / Frontal Pole	**0.77**	0.01
L Anterior Insula	**0.64**	0.12
R Midcingulate Cortex	**0.64**	0.21
R Frontal Operculum	**0.62**	0.08
R Anterior Insula	**0.42**	0.35
R Bed Nucleus of the Stria Terminalis	-0.02	**0.83**
R Amygdala	-0.03	**0.81**
L Bed Nucleus of the Stria Terminalis	0.08	**0.77**
L Amygdala	0.02	**0.76**
Periaqueductal Gray	0.31	**0.42**

Table S2. Descriptive statistics for clusters and local maxima showing greater activity during the anticipation of Threat compared to Safety (FDR *q*<.05, whole-brain corrected).

mm³	Region	*t*	*x*	*y*	*z*
1,328,072	L Dorsolateral Prefrontal Cortex/Frontal Pole[a]	15.05	-30	50	30
	R Dorsolateral Prefrontal Cortex/Frontal Pole[a]	13.40	34	48	30
	L Middle Frontal Gyrus	13.01	-36	34	36
	R Middle Frontal Gyrus	3.79	48	22	44
	L Frontal Orbital Cortex (Basal Operculum)	16.11	-34	28	-4
	R Frontal Orbital Cortex (Basal Operculum)	16.60	36	28	0
	L Anterior Insula (Anterior Insular Point)[a]	16.71	-30	26	4
	R Anterior Insula (Orbitoinsularis Cortex)[a]	13.40	32	22	-10
	R Midcingulate Cortex (Cingulate Gyrus, Cingulate Sulcus)[a]	17.08	8	20	34
	L Midcingulate Cortex (Paracingulate Gyrus)[a]	16.47	-4	8	42
	R Frontal Operculum (Op 8)[a]	18.23	46	18	2
	L Frontal Operculum (Op 8)[a]	19.43	-40	14	2
	R Inferior Frontal Gyrus, pars opercularis	9.12	38	14	24
	R Caudate	14.31	18	12	12
	R Putamen	17.57	24	10	0
	L Putamen	15.42	-22	8	0
	L Temporal Pole	5.79	-40	10	-38
	R Temporal Pole	9.71	44	6	-38
	L Bed Nucleus of Stria Terminalis[a,b]	9.61	-8	4	0
	R Bed Nucleus of Stria Terminalis[a,b]	7.28	8	4	2

R Superior Temporal Gyrus, anterior division	3.00	54	4	-14
L Superior Frontal Gyrus	15.81	-14	2	68
R Juxtapositional Lobule	17.44	4	6	54
L Juxtapositional Lobule	15.39	-6	2	52
L Inferior Temporal Gyrus, anterior division	6.30	-50	0	-34
R Precentral Gyrus	16.31	46	0	50
L Amygdala[a,c] (Medial Nucleus)	5.93	-22	-2	-12
L Caudate	14.15	-14	-2	16
R Superior Frontal Gyrus	16.67	12	-2	72
R Amygdala[a,d] (Central, Medial Nuclei)	8.03	22	-2	-12
L Planum Polare	4.76	-42	-4	-18
L Parahippocampal Gyrus, anterior division	6.82	-26	-4	-32
L Precentral Gyrus	13.42	-34	-6	60
R Parahippocampal Gyrus, anterior division	4.47	24	-6	-32
L Pallidum	12.81	-18	-10	0
R Thalamus	13.10	16	-10	6
L Thalamus	8.50	-6	-20	16
R Planum Polare	5.77	42	-10	-12
R Pallidum	11.98	26	-12	2
L Temporal Fusiform Cortex, posterior	2.74	-32	-14	-42
R Temporal Fusiform Cortex, posterior	2.53	42	-28	-28
R Posterior Cingulate Cortex	12.35	8	-20	40
L Posterior Cingulate Cortex	13.23	-10	-24	38
L Brain Stem	12.87	-10	-24	-18
R Brain Stem	14.18	8	-30	-14
R Parietal Operculum	11.95	54	-24	22
L Inferior Temporal Gyrus, posterior	4.03	-60	-28	-22
R Inferior Temporal Gyrus, posterior	3.70	52	-32	-28
R Postcentral Gyrus	10.93	46	-28	48
R Periaqueductal Gray[a]	10.23	4	-30	-6
R Middle Temporal Gyrus, posterior	13.40	50	-30	-6
L Middle Temporal Gyrus, posterior	6.91	-60	-32	-8
R Hippocampus, posterior	7.39	34	-32	-4
L Postcentral Gyrus	10.21	-42	-34	46
R Supramarginal Gyrus, posterior	16.44	60	-42	34
L Supramarginal Gyrus, posterior	16.34	-58	-48	34
L Inferior Temporal Gyrus, temporooccipital	3.71	-60	-46	-20
R Inferior Temporal Gyrus, temporooccipital	6.63	54	-60	-14
R Superior Parietal Lobule	13.07	24	-48	66
L Angular Gyrus	9.98	-50	-54	50
L Superior Parietal Lobule	10.7	-34	-54	62
L Precuneus	10.14	-10	-56	60

	R Precuneus Cortex	10.20	10	-58	60
	R Middle Temporal Gyrus, temporooccipital	9.67	44	-56	8
	L Middle Temporal Gyrus, temporooccipital	9.02	-46	-60	10
	L Lateral Occipital Cortex, superior	10.27	-32	-60	60
	R Lateral Occipital Cortex, superior	9.08	28	-62	60
	R Lateral Occipital Cortex, inferior	8.36	48	-70	-12
	L Lateral Occipital Cortex, inferior	5.11	-44	-84	-4
	L Lingual Gyrus	7.18	-12	-86	-12
	R Occipital Fusiform Gyrus	4.69	22	-88	-6
	L Occipital Pole	6.56	-18	-90	26
	R Occipital Pole	8.54	28	-90	10
56	R Frontal Pole	2.20	10	74	8
8	R Inferior Temporal Gyrus, posterior	1.87	54	-18	-30

[a] Region used in EMA analyses. [b] Overlaps the BST sub-region anatomically defined by Theiss and colleagues (Theiss, Ridgewell, McHugo, Heckers, & Blackford, 2017). [c] Harvard-Oxford left amygdala, p=36%. [c] Harvard-Oxford right amygdala, p=56%.

Table S3. Descriptive statistics for clusters and local maxima showing greater activity during threat-related faces compared to places (FDR q<.05, whole-brain corrected).

mm³	Region	t	x	y	z
1,440,200	R Frontal Pole	11.42	4	58	24
	L Frontal Pole	8.8	-34	52	26
	R Frontal Medial Cortex	13.57	4	54	-14
	L Frontal Medial Cortex	12.4	-4	50	-16
	R Inferior Frontal Gyrus, pars triangularis	11.6	56	34	6
	L Inferior Frontal Gyrus, pars triangularis	6.04	-54	30	4
	R Frontal Operculum	9.81	46	26	0
	R Middle Frontal Gyrus	6.15	46	26	44
	L Middle Frontal Gyrus	16.75	-34	-4	60
	R Pregenual Anterior Cingulate Cortex	9.24	10	46	-4
	L Midcingulate Cortex (Paracingulate Gyrus)	12.64	-2	20	38
	L Midcingulate Cortex (Cingulate Sulcus)	11.59	-6	22	30
	R Midcingulate Cortex (Cingulate Gyrus)	12.17	6	16	34
	R Accumbens	7.58	12	20	-6
	L Accumbens	7.42	-10	16	-6
	R Inferior Frontal Gyrus, pars opercularis	11.57	46	16	28
	L Inferior Frontal Gyrus, pars opercularis	9.03	-46	16	26

R Frontal Orbital Cortex (Gustatory Cortex)	12.26	26	14	-20
L Frontal Orbital Cortex / Insula	11.9	-28	14	-16
L Superior Frontal Gyrus	10.75	-12	10	66
R Temporal Pole	10.4	36	4	-40
L Temporal Pole	13.6	-34	4	-20
R Middle Temporal Gyrus, anterior	5.79	50	2	-30
L Middle Temporal Gyrus, anterior	5.73	-62	0	-18
R Insula	16.44	38	2	-18
L Insula	14.11	-38	0	-16
L Superior Temporal Gyrus, anterior	5.48	-52	2	-16
R Precentral Gyrus	18.73	46	-2	50
R Temporal Fusiform Cortex, anterior	10.55	32	-2	-38
L Pallidum	7.19	-14	-2	-2
L Putamen	10.22	-24	-2	4
R Putamen	12.18	30	-22	2
L Parahippocampal Gyrus, anterior	10.76	-30	-2	-34
L Juxtapositional Lobule	19.21	-2	-8	68
R Juxtapositional Lobule	17.24	0	-4	60
R Amygdala[a,b] (Medial Nucleus)	25.76	22	-6	-14
L Amygdala[a,c] (Medial Nucleus)	22.78	-20	-6	-14
R Caudate	12.05	16	-6	20
L Central Operculum	9.82	-40	-6	14
L Caudate	12.8	-16	-8	20
R Superior Frontal Gyrus	16.69	20	-10	72
L Thalamus	14.65	-2	-12	6
R Thalamus	16.07	6	-16	8
L Precentral Gyrus	20.3	-44	-12	54
R Middle Temporal Gyrus, posterior	13.37	48	-18	-10
R Posterior Cingulate Cortex	13.35	2	-18	32
L Posterior Cingulate Cortex	13.71	-10	-22	42
R Planum Polare	4.44	40	-20	-2
R Inferior Temporal Gyrus, posterior	4	48	-22	-26
L Inferior Temporal Gyrus, posterior	2.18	-62	-42	-24
L Superior Temporal Gyrus, posterior	8.83	-54	-22	-4
R Supramarginal Gyrus, anterior	12.56	52	-24	40
L Postcentral Gyrus	20.04	-42	-24	54
R Postcentral Gyrus	16.84	12	-32	72
L Hippocampus	5.92	-26	-28	-12
R Hippocampus	6.92	26	-38	-4
L Parietal Operculum	10.94	-44	-28	16
R Parietal Operculum	13.08	62	-32	26
R Brain Stem	8.75	8	-30	-6
L Brain Stem	7.47	-6	-34	-44
L Middle Temporal Gyrus, posterior	7.51	-62	-32	0

R Planum Temporale	8.17	40	-34	16
R Supramarginal Gyrus, posterior	18.17	54	-40	10
L Supramarginal Gyrus, posterior	11.6	-56	-42	24
L Superior Parietal Lobule	19.13	-34	-44	62
R Superior Parietal Lobule	14.83	24	-48	68
L Temporal Occipital Fusiform Cortex	18.72	-42	-48	-20
R Angular Gyrus	8.34	62	-50	42
L Angular Gyrus	8.25	-54	-52	46
R Temporal Occipital Fusiform Cortex	16.89	44	-54	-20
R Precuneus	15.7	6	-54	24
L Precuneus	11.39	-6	-58	42
R Lateral Occipital Cortex, superior	5.97	24	-60	64
L Lateral Occipital Cortex, superior	8.87	-46	-62	48
L Lateral Occipital Cortex, inferior	19.58	-48	-66	10
R Lateral Occipital Cortex, inferior	20.95	50	-62	6
R Lingual Gyrus	15.93	12	-62	-2
L Lingual Gyrus	22.34	-6	-74	4
R Intracalcarine Cortex	21.86	6	-70	8
R Supracalcarine Cortex	20.60	0	-74	12
L Supracalcarine Cortex	21.08	-2	-84	12
L Occipital Fusiform Gyrus	5.97	-40	-74	-16
R Cuneus	14.09	2	-80	30

[a] Region used in EMA analyses. [c] Harvard-Oxford right amygdala, p=99%. [c] Harvard-Oxford left amygdala, p=98%.

Table S4. Relations between frontocortical reactivity to threat anticipation and real-world negative affect, controlling for subcortical reactivity.

	t	β
Threat-Anticipation Frontocortical Composite[a]	-0.37	-0.02
Stressor (vs. Absent)	15.12***	0.34
Threat-Anticipation Frontocortical Composite[a] × Stressor	-2.43*	-0.09
Threat-Anticipation Subcortical Composite	0.60	0.02
Threat-Anticipation Subcortical Composite × Stressor	0.89	0.03

[a] The *Composite* term tests relations between frontocortical function and tonic (stressor-independent) negative affect. The *Composite × Stressor* term tests relations between frontocortical function and reactive (stressor-dependent) negative affect. * $p \leq 0.05$, ** $p < 0.01$, *** $p < 0.001$

Continued...

Table S5. Relations between frontocortical reactivity to threat anticipation and real-world anxiety and depression.

	Anxiety		Depression	
	t	β	t	β
Threat-Anticipation Frontocortical Composite[a]	-0.26	-0.01	0.40	0.01
Stressor (vs. Absent)	12.73***	0.34	12.74***	0.35
Threat-Anticipation Frontocortical Composite[a] × Stressor	-1.95*	-0.07	-2.04*	-0.07

[a] The *Composite* term tests relations between frontocortical function and tonic (stressor-independent) anxiety or depression. The *Composite × Stressor* term tests relations between frontocortical function and reactive (stressor-dependent) anxiety or depression. * $p \leq 0.05$, ** $p < 0.01$, *** $p < 0.001$

Table S6. Relations between frontocortical reactivity to threat anticipation and real-world negative affect, controlling for stressor frequency.

	t	β
Threat-Anticipation Frontocortical Composite[a]	0.02	0.00
Stressor (vs. Absent)	14.83***	0.34
Threat-Anticipation Frontocortical Composite[a] × Stressor	-2.42*	-0.07
Stressor Frequency	2.62**	0.06

[a] The *Composite* term tests relations between frontocortical function and tonic (stressor-independent) negative affect. The *Composite × Stressor* term tests relations between frontocortical function and reactive (stressor-dependent) negative affect. * $p \leq 0.05$, ** $p < 0.01$, *** $p < 0.001$

Table S7. Relations between frontocortical reactivity to threat anticipation and real-world negative affect, controlling for amygdala reactivity to threat-related faces.

	t	β
Threat-Anticipation Frontocortical Composite[a]	-0.34	-0.01
Stressor (vs. Absent)	15.00***	0.35
Threat-Anticipation Frontocortical Composite[a] × Stressor	-2.21*	-0.07
Threat-Related Faces Amygdala Composite	-0.45	-0.01
Threat-Related Faces Amygdala Composite × Stressor	-1.56	-0.04

[a] The *Composite* term tests relations between frontocortical function and tonic (stressor-independent) negative affect. The *Composite × Stressor* term tests relations between frontocortical function and reactive (stressor-dependent) negative affect. * $p \leq 0.05$, ** $p < 0.01$, *** $p < 0.001$

Continued...

Table S8. Relations between frontocortical reactivity to threat anticipation and real-world positive affect.

	t	*β*
Threat-Anticipation Frontocortical Composite[a]	0.95	0.05
Positive Event (vs. Absent)	23.77***	0.51
Threat-Anticipation Frontocortical Composite[a] × Positive Event	-1.46	-0.04

[a] The *Composite* term tests relations between frontocortical function and tonic (stressor-independent) *positive* affect. The *Composite × Stressor* term tests relations between frontocortical function and reactive (stressor-dependent) *positive* affect. * $p \leq 0.05$, ** $p < 0.01$, *** $p < 0.001$

Table S9. Relations between frontocortical reactivity to threat anticipation and real-world negative affect, controlling for individual differences in trait negative emotionality.

	t	*β*
Threat-Anticipation Frontocortical Composite[a]	0.18	0.01
Stressor (vs. Absent)	15.87***	0.35
Threat-Anticipation Frontocortical Composite[a] × Stressor	-2.17*	-0.06
Trait Negative Emotionality	4.21**	0.10
Trait Negative Emotionality × Stressor	4.53***	0.11

[a] The *Composite* term tests relations between frontocortical function and tonic (stressor-independent) negative affect. The *Composite × Stressor* term tests relations between frontocortical function and reactive (stressor-dependent) negative affect. * $p \leq 0.05$, ** $p < 0.01$, *** $p < 0.001$

Table S10. Relations between regional frontocortical reactivity to threat anticipation and real-world negative affect.

	Threat-Anticipation dlPFC/FP		Threat-Anticipation FrO		Threat-Anticipation AI		Threat-Anticipation MCC	
	t	*β*	*t*	*β*	*t*	*β*	*t*	*β*
Brain[a]	0.53	0.02	-0.78	-0.02	0.84	0.02	-0.59	-0.02
Stressor (vs. Absent)	15.02***	0.34	15.14***	0.34	14.98***	0.34	15.17***	0.34
Brain[a] × Stressor	-1.39	-0.03	-2.56*	-0.06	-1.59	-0.04	-2.63**	-0.07

[a] Focal neural metric. The *Brain* term tests relations between regional brain function and tonic (stressor-independent) negative affect. The *Composite × Stressor* term tests relations between regional brain function and reactive (stressor-dependent) negative affect. * $p \leq 0.05$, ** $p < 0.01$, *** $p < 0.001$

Continued…

Table S11. Relations between MCC reactivity to threat anticipation and real-world negative affect, controlling for AI and dlPFC/FP reactivity.

	t	*β*
MCC Threat-Anticipation[a]	-1.76	-0.07
Stressor (vs. Absent)	15.06***	0.35
MCC Threat-Anticipation[a] × Stressor	-2.05*	-0.08
AI Threat-Anticipation	1.34	0.05
AI Threat-Anticipation × Stressor	-0.10	0.04
dlPFC Threat-Anticipation	1.03	0.04
dlPFC Threat-Anticipation × Stressor	0.58	0.02

[a] The *MCC* term tests relations between MCC function and tonic (stressor-independent) negative affect. The *MCC × Stressor* term tests relations between MCC function and reactive (stressor-dependent) negative affect. * $p \leq 0.05$, ** $p < 0.01$, *** $p < 0.001$

Table S12. Relations between FrO reactivity to threat anticipation and real-world negative affect, controlling for AI and dlPFC/FP reactivity.

	t	*β*
FrO Threat-Anticipation[a]	-1.96*	-0.08
Stressor (vs. Absent)	15.05***	0.34
FrO Threat-Anticipation[a] × Stressor	-1.94*	-0.07
AI Threat-Anticipation	1.54	0.06
AI Threat-Anticipation × Stressor	0.13	0.00
dlPFC Threat-Anticipation	0.39	0.03
dlPFC Threat-Anticipation × Stressor	0.80	0.01

[a] The *FrO* term tests relations between FrO function and tonic (stressor-independent) negative affect. The *FrO × Stressor* term tests relations between FrO function and reactive (stressor-dependent) negative affect. * $p \leq 0.05$, ** $p < 0.01$, *** $p < 0.001$

Table S13. Relations between MCC and FrO reactivity to threat anticipation and real-world negative affect, controlling for the other region.

	t	*β*
MCC Threat-Anticipation[a]	-0.04	-0.00
Stressor (vs. Absent)	15.14	0.34
MCC Threat-Anticipation[a] × Stressor	-1.07	-0.04
FrO Threat-Anticipation[b]	-0.51	-0.02
FrO Threat-Anticipation[b] × Stressor	-0.95	-0.03

[a] The *MCC* term tests relations between MCC function and tonic (stressor-independent) negative affect. The *MCC × Stressor* term tests relations between MCC function and reactive (stressor-dependent) negative affect. [b] The *FrO* term tests relations between FrO function and tonic (stressor-independent) negative affect. The *FrO × Stressor* term tests relations between FrO function and reactive (stressor-dependent) negative affect. * $p \leq 0.05$, ** $p < 0.01$, *** $p < 0.001$

Continued…

Supplementary Method for Meta-Analytic Analyses of the Cingulo-Opercular Circuit

Neurosynth—a cloud-based suite of neuroinformatics tools and databases—was used to clarify the functional architecture of regions highlighted by our Brain-EMA results (Yarkoni, Poldrack, Nichols, Van Essen, & Wager, 2011).

Functional connectivity. Intrinsic functional connectivity was assessed using an automated seed-based approach and data from the Yeo-Buckner database, which incorporates 'resting-state' fMRI data from 1,000 participants (Yeo et al., 2011). For illustrative purposes, connectivity maps were arbitrarily thresholded at a conservative level ($p < 1.76 \times 10^{-10}$, uncorrected).

Meta-analytic co-activation. Regional co-activation patterns were meta-analytically assessed using an automated seed-based approach and a database of >500,000 stereotactic coordinates from >14,000 published imaging studies. Meta-analytic co-activation maps were thresholded using FDR $q < .01$ (whole-brain corrected).

Meta-Analytic Results

The present results raise the possibility that the MCC and FrO represent a meaningful functional circuit. If so, then we would expect them to show robust intrinsic functional connectivity in the absence of an explicit task *and* a consistent pattern of co-activation across experimental challenges (Laird et al., 2013; Yeo et al., 2011). We used Neurosynth—a cloud-based suite of neuroinformatics tools and databases—to test these two predictions (Yarkoni et al., 2011). We began by assessing the intrinsic functional connectivity of the MCC and FrO in the Yeo-Buckner database (n = 1,000; Yeo et al., 2011), using the peak locations identified in the threat-anticipation task as seeds (cf. **Figure 2c** in the main report). In each case, there was

substantial functional connectivity with the other seed locations (e.g., right MCC ↔ left FrO; $p < 1.76 \times 10^{-10}$, uncorrected; **Supplementary Figure S3a**).

We used a conceptually similar seed-based approach to probe MCC-FrO co-activation. This analysis leveraged a computer-generated database of >500,000 stereotactic coordinates derived from >14,000 published imaging studies. This allowed us to perform a series of automated meta-analyses, each quantifying the likelihood that activation in any one of the seed locations is associated with significant co-activation in the other three (FDR $q < .01$, whole-brain corrected). Mirroring the functional connectivity results, this revealed robust co-activation across the four seed locations (Supplementary **Figure S3b**).
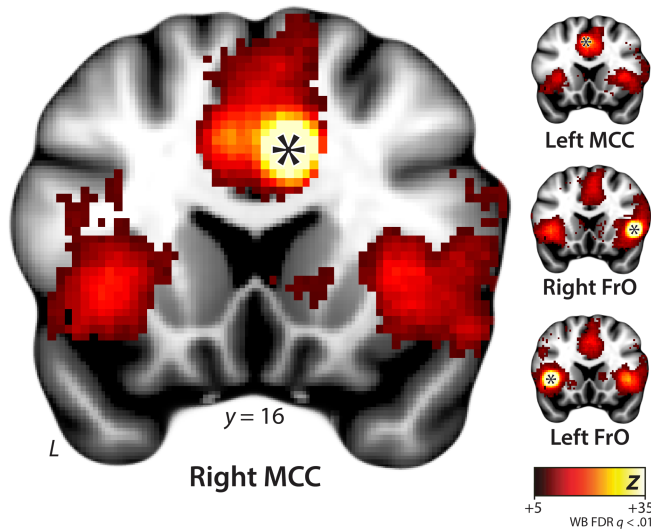
Taken together, these results provide clear evidence that the MCC and FrO form a cingulo-opercular circuit that is sensitive to threat-anticipation in the laboratory and associated with dampened stressor reactivity in the real world.

Continued…

a. Functional connectivity
Yeo-Buckner database (*n* = 1,000)

y = 16
L
Right MCC

Left MCC

Right FrO

Left FrO

r
+0.20   +1
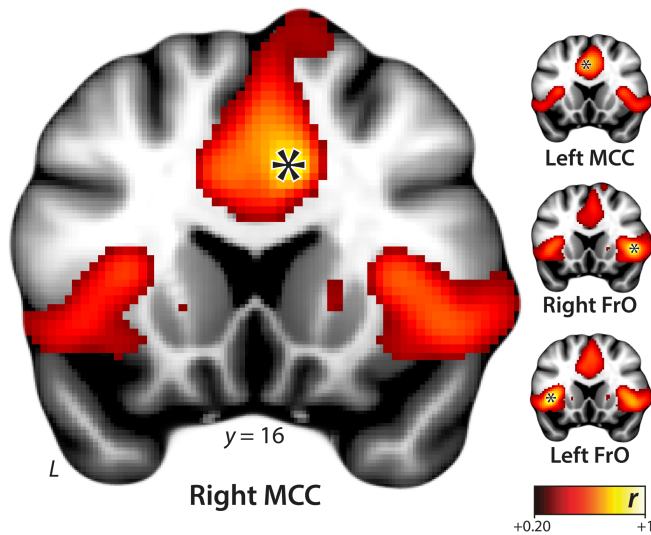
b. Co-activation
Neurosynth automated meta-analysis (*k* = 14,371)

y = 16
L
Right MCC

Left MCC

Right FrO

Left FrO

z
+5   +35
WB FDR *q* < .01

Supplementary Figure S3. **The MCC and FrO form a coherent functional neuroanatomical circuit.** Asterisks depict the approximate location of each seed. **a. Functional connectivity.** Panel depicts the results of seed-based analyses of intrinsic functional connectivity between the MCC and FrO. Analyses were performed using Neurosynth and the Yeo-Buckner database of 1,000 'resting' fMRI assessments. See **Supplementary Table S1** for seed coordinates. Connectivity maps are shown using an arbitrary threshold (*p* < 1.76 × 10^{-10}, uncorrected). **b. Co-activation.** Panel depicts the results of seed-based co-activation meta-analyses. Meta-analyses were automatically computed using the Neurosynth database, which encompasses peak coordinates from >15,000 published neuroimaging studies. Co-activation maps are depicted using a FDR *q* < .01, whole-brain corrected threshold. **Abbreviations**—FDR, false discovery rate; FrO, frontal operculum; *k*, the number of studies used in the meta-analysis; L, left; MCC, midcingulate cortex; WB, whole-brain corrected.

Continued…

Supplementary References

Choi, J. M., Padmala, S., & Pessoa, L. (2012). Impact of state anxiety on the interaction between threat monitoring and cognition. *NeuroImage, 59*(2), 1912-1923.

Choi, J. M., Padmala, S., & Pessoa, L. (2015). Counteracting effect of threat on reward enhancements during working memory. *Cognition and Emotion, 29*(8), 1517-1526.

Ebner, N. C., Riediger, M., & Lindenberger, U. (2010). FACES—A database of facial expressions in young, middle-aged, and older women and men: Development and validation. *Behavior research methods, 42*(1), 351-362.

Ekman, P., & Friesen, W. (1976). Pictures of Facial Affect (Palo Alto, CA: Consulting Psychologists).

Gamer, M., Schmitz, A. K., Tittgemeyer, M., & Schilbach, L. (2013). The human amygdala drives reflexive orienting towards facial features. *Current Biology, 23*(20), R917-R918.

Henson, R. (2007a). Efficient experimental design for fMRI. In K. Friston, J. Ashburner, S. Kiebel, T. Nichols, & W. Penny (Eds.), *Statistical parametric mapping: The analysis of functional brain images* (pp. 193-210). New York, NY: Academic Press.

Henson, R. (2007b). Efficient experimental design for fMRI. *Statistical parametric mapping: The analysis of functional brain images*, 193-210.

Hur, J., Smith, J. F., DeYoung, K. A., Anderson, A. S., Kuang, J., Kim, H. C., . . . Shackman, A. J. (2020). Anxiety and the neurobiology of temporally uncertain threat anticipation. *Journal of Neuroscience, 40*, 7949-7964. doi:10.1101/2020.02.25.964734

Laird, A. R., Eickhoff, S. B., Rottschy, C., Bzdok, D., Ray, K. L., & Fox, P. T. (2013). Networks of task co-activations. *Neuroimage, 80*, 505-514. doi:10.1016/j.neuroimage.2013.04.073

Maus, B., van Breukelen, G. J., Goebel, R., & Berger, M. P. (2010). Optimization of blocked designs in fMRI studies. *Psychometrika, 75*(2), 373-390.

Plichta, M. M., Grimm, O., Morgen, K., Mier, D., Sauer, C., Haddad, L., . . . Schwarz, A. J. (2014). Amygdala habituation: a reliable fMRI phenotype. *Neuroimage, 103*, 383-390.

Scheller, E., Büchel, C., & Gamer, M. (2012). Diagnostic features of emotional expressions are processed preferentially. *PLoS One, 7*(7), e41792.

Theiss, J. D., Ridgewell, C., McHugo, M., Heckers, S., & Blackford, J. U. (2017). Manual segmentation of the human bed nucleus of the stria terminalis using 3T MRI. *Neuroimage, 146*, 288-292. doi:10.1016/j.neuroimage.2016.11.047

Yarkoni, T., Poldrack, R. A., Nichols, T. E., Van Essen, D. C., & Wager, T. D. (2011). Large-scale automated synthesis of human functional neuroimaging data. *Nat Methods, 8*, 665-670. doi:nmeth.1635 [pii] 10.1038/nmeth.1635

Yeo, B. T., Krienen, F. M., Sepulcre, J., Sabuncu, M. R., Lashkari, D., Hollinshead, M., . . . Buckner, R. L. (2011). The organization of the human cerebral cortex estimated by intrinsic functional connectivity. *J Neurophysiol, 106*, 1125-1165. doi:10.1152/jn.00338.2011